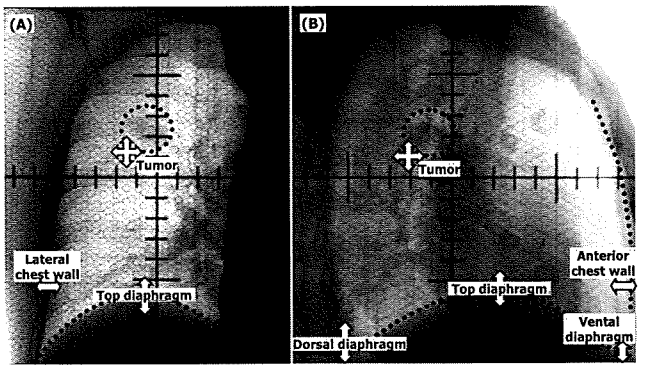

FIG. 2. Orthogonally acquired frontal (a) and lateral (b) fluoroscopic images used to obtain respiratory motion data for lung tumors and other anatomical structures. Arrows indicate the positions of the observation points used to collect motion data for essential anatomical structures (i.e., the tumor, anterior/lateral chest wall, and dorsal/ventral/top diaphragm position). The position of the top of the diaphragm dome was used as the surrogate breathing signal.

can be estimated from that of the diaphragm. The entire configurations of the diaphragm and chest wall can be estimated from the position of just a few points. Because most major movements can be represented by the position of the diaphragm and chest wall, the observation points include tumor position (in the RL and SI directions), the lateral position of the chest wall, and the top positions of the right/left diaphragm dome (in the SI direction); these points are monitored through anterioposterior fluoroscopic imaging. Lateral fluoroscopic imaging is used to track the tumor position in the AP and SI directions, the anterior position of the chest

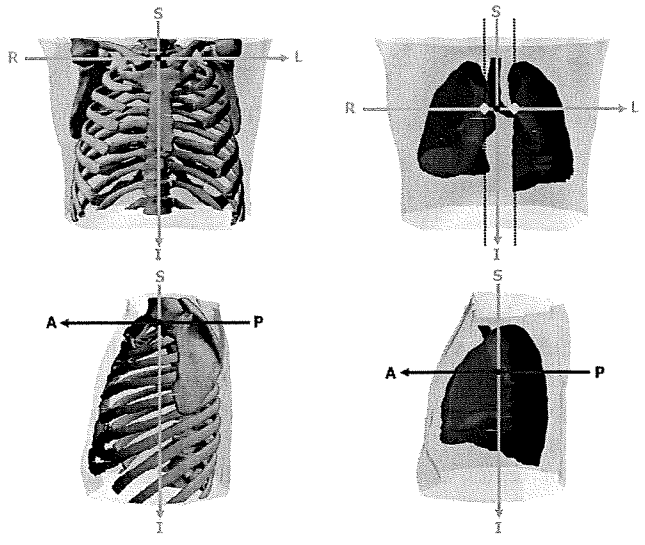

FIG. 3. A schematic of the (a) thoracic wall coordinate system and (b) the thoracic cage coordinate system. The origin of the coordinate system for the thoracic wall was positioned at the intersection point of the horizontal plane at the lung apex and the midcoronal and midsagittal planes. For the thoracic cage, the origins were defined separately for the right and left lungs (indicated by rhombus marks). They were pointed at the midpoint of the lungs in the AP direction, at the side of the mediastinum in the RL direction, and at the superior position of the tracheal bifurcation in the SI direction.

wall, and the dorsal/ventral/top diaphragm positions (in the SI direction). As it is difficult to identify and track a specific point on the chest wall, we measured the magnitude of the changes in the anterioposterior and lateral diameters of the thoracic cage in the same plane in orthogonal radiographs as a substitute for the chest wall position. These measuring planes were set at the diaphragm dome level in 3D-CT.

As for the observation points of the tumor, their motion was assessed as that of the whole volume by tracking the tumor region on fluoroscopy. Because the right diaphragm is positioned higher than the left, lateral fluoroscopic imaging generally shows the right diaphragm. Therefore, in the case of left lung tumors, the top positions of the right and left diaphragm domes are measured via anteroposterior fluoroscopic imaging. To obtain 3D motion data, simultaneous fluoroscopic acquisition from two directions is required. However, because the x-ray fluoroscope at our institution could not acquire images simultaneously, the top position of the diaphragm dome was used to synchronize the breathing phase between image sets.

The type of deformation differs inside versus outside of the thoracic cage, as described above; therefore, the transformation vectors are computed separately. A schematic of the different coordinate systems and an explanation of how to compute the transformation map are presented in Figs. 3 and 4. The region of the thoracic cage was determined from the contours of the right and left lungs and the vertebrae, that is, by removing the vertebrae from the region configured by connecting contours of right and left lungs. For points outside of the thoracic cage, the value of transformation vectors depended on movements of the chest wall alone, which are determined via fluoroscopic imaging. The thoracic wall is divided into three regions (i.e., the anterior, posterior, and side thoracic wall) and a different calculation method is used to determine transformation vectors for each region.

First, in our algorithm, the sternum was deemed as a rigid body; therefore, it can be handled with an affine transformation. The upper part of the anterior thoracic wall is generally less mobile than the lower part. In addition, lateral motion of the thoracic wall is very slight. Therefore, the anterior thoracic wall is assumed to show rotational motion in the sagittal plane, and its rotational axis is set at the intersection of the horizontal plane at lung apex and the midcoronal plane. The lateral expansion of the thoracic wall is typically small, so lateral motion is addressed using additional component of translational scaling. Its value is set at 0 around the sternum and is increased or decreased linearly from the center of the lungs to each side of the body. Therefore, transformation vectors at the anterior thoracic wall consist of a combination of rotational and translational vectors, as shown in the following equation:

$$\mathbf{T}_i(\mathbf{r}) = \mathbf{Rot}_i(\mathbf{r}) + \mathbf{Trans}_i(\mathbf{r}) \quad \text{if } \mathbf{r} \in \text{anterior thoracic wall.} \tag{3}$$

The rotational component of transformation vector ($\mathbf{Rot}_i$) is calculated using the unit vector for x-axis rotation ($\mathbf{Rot}_x$),

$$\mathbf{Rot}_i(\mathbf{r}) = \mathbf{Rot}_x(\mathbf{r}) - \mathbf{r},$$

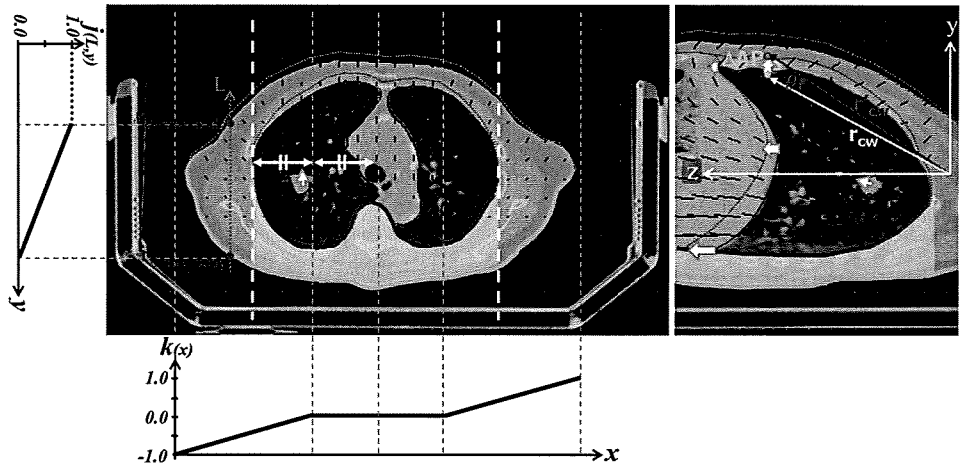

FIG. 4. Computing the transformation map required to create 3D-CT images for an arbitrary breathing phase. For points outside of the thoracic cage, transformation vectors in the anterior thoracic wall were determined by sagittal rotation (θ) and lateral linear scaling [$k(x)$]. The rotational axis was set at the intersection of the horizontal plane at the lung apex and the midcoronal plane. $\mathbf{r}_{CW}, \mathbf{r}'_{CW}$ indicates the position of the observation point in the anterior chest wall in the original CT phase and selected phase i. $\mathbf{r}'_{CW}$ was calculated from the AP motion of the chest wall (ΔAP), as observed via fluoroscopic imaging. The coefficient function $k(x)$ has a zero band, which is set to half the size of the thoracic cage in the middle to avoid scaling of sternum. The posterior thoracic wall (shaded area around thoracic vertebra) and body surface in contact with immobilization device (shown as a thick green line) were assumed to be fixed. Also, vectors in the side thoracic wall were linearly interpolated [$j(L,y)$] from the vectors of points on the ventral and dorsal body surfaces. Inside the thoracic cage, transformation vectors were determined by incorporating the vector element of tumor motion into the vector posed by scaling in each direction.

$$\mathbf{Rot}_i(\mathbf{r}) = \begin{bmatrix} 1 & 0 & 0 \\ 0 & \cos\theta & -\sin\theta \\ 0 & \sin\theta & \cos\theta \end{bmatrix} \cdot \begin{bmatrix} x \\ y \\ z \end{bmatrix} - \begin{bmatrix} x \\ y \\ z \end{bmatrix} = \begin{bmatrix} 0 \\ (z\cdot\sin\theta + y\cdot\cos\theta) - y \\ (z\cdot\cos\theta - y\cdot\sin\theta) - z \end{bmatrix}. \quad (4)$$

The rotational angle (θ) is determined by the position of the observation point $\mathbf{r}_{CW}, \mathbf{r}'_{CW}$ in the anterior chest wall in the original CT phase and selected phase i,

$$\mathbf{r}'_{CW} = \mathbf{r}_{CW} + (0, \Delta AP, 0),$$

$$\cos\theta = \frac{\mathbf{r}_{CW}\cdot\mathbf{r}'_{CW}}{|\mathbf{r}_{CW}|\cdot|\mathbf{r}'_{CW}|}, \quad (5)$$

where ΔAP is the anteroposterior motion of the chest wall observed via fluoroscopic imaging. The translational scaling component of the vector ($\mathbf{Trans}_i$) is calculated from the lateral motion of the chest wall (ΔRL) as observed via fluoroscopic imaging and the coefficient function $k(x)$ indicated in Fig. 4,

$$\mathbf{Trans}_i(\mathbf{r}) = \begin{bmatrix} k(x)\times\Delta RL \\ 0 \\ 0 \end{bmatrix}. \quad (6)$$

To avoid scaling of the sternum, which affects the dose calculation, $k(x)$ has a zero band in the middle. Its interval was set to half the size of the thoracic cage to sufficiently include the sternum.

Second, the posterior thoracic wall is considered to be stationary, and the vector values are set to 0,

$$\mathbf{T}_i(\mathbf{r}) = 0 \quad \text{if } \mathbf{r} \in \text{posterior thoracic wall}. \quad (7)$$

Finally, in the side thoracic wall, the vector values of points on the ventral body surface are determined in the same way as points in the anterior thoracic wall [Eq. (3)], and points on the dorsal body surface, which is in direct contact with the immobilization device (i.e., the vacuum pillow), are assumed to be fixed [Eq. (7)]. The transformation vectors of other points are linearly interpolated from the vectors of points on the ventral and dorsal body surfaces on the same line in the AP direction based on the following equation:

$$\mathbf{T}_i(\mathbf{r}) = \mathbf{T}_i(\mathbf{r}_{\text{ventral body}})\times j(L,y) + \mathbf{T}_i(\mathbf{r}_{\text{dorsal body}})\times(1 - j(L,y)) \quad \text{if } \mathbf{r} \in \text{side thoracic wall}, \quad (8)$$

where $\mathbf{r}_{\text{ventral body}}$ and $\mathbf{r}_{\text{dorsal body}}$ are the transformation vectors at the intersectional position of the dorsal-ventral line (L) and the body surface, respectively. $\mathbf{T}_i(\mathbf{r}_{\text{dorsal body}})$ is always 0, and $j(L,y)$ is defined with respect to each line (L).

On the other hand, transformation vectors inside the thoracic cage are defined by movement at all observation points, including the tumor. The thoracic cage, with the exception of the tumor region contoured on the 3D-CT, is assumed to expand or contract in a linear fashion from the origin, which is positioned at the midpoint of the lungs in the AP direction, at the side of the mediastinum in the RL direction, and at the superior position of the tracheal bifurcation in the SI direction. Only the SI position is manually selected; the AP and RL positions will be set automatically in the slice of the selected level. The tumor volume is assumed to move rigidly, without deformation, so the vector values of points inside the tumor region are set to the values assessed by fluoroscopy. Accordingly, the transformation vectors of points inside the

thoracic cage are determined by incorporating the vector element of tumor motion into the vector posed by scaling in each direction as follows:

$$\mathbf{T}_i(\mathbf{r}) = \{\boldsymbol{\varepsilon}_{\mathrm{AP}}(\mathbf{r}) + \boldsymbol{\varepsilon}_{\mathrm{RL}}(\mathbf{r}) + \boldsymbol{\varepsilon}_{\mathrm{SI}}(\mathbf{r})\} \times (1 - l) + \mathbf{T}_i(\mathbf{r}_{\mathrm{tumor}}) \times l \quad \text{if } \mathbf{r} \in \text{inside the thoracic cage}, \tag{9}$$

where $\boldsymbol{\varepsilon}_{\mathrm{AP}}(\mathbf{r})$, $\boldsymbol{\varepsilon}_{\mathrm{RL}}(\mathbf{r})$, and $\boldsymbol{\varepsilon}_{\mathrm{SI}}(\mathbf{r})$ are the vectors posed by the scaling in the AP, RL, and SI directions, respectively, which depend on the movement of observation points in the anterior chest wall, lateral chest wall, and diaphragm, respectively. Specifically, the SI component of transformation is determined initially. The vector value of the SI component is set to 0 at the upper area, relative to the origin position. At the level under the diaphragm observation point, the vector value is determined according to the y position, from the dorsal/ventral/top diaphragm movements by using linear interpolation. At the other area, the vector value is linearly interpolated according to the z position, from vectors at the level of the diaphragm and the origin (i.e., 0). After deformation in the SI direction is performed, the AP and RL components of transformation are determined by expanding or shrinking the thoracic cage to conform to the precalculated deformed boundary of the chest wall in each slice, perpendicular to the z axis. Then, the lateral components of transformation vectors are set to 0 in the mediastinal space, which was defined as the region of the thoracic cage excluding the lungs. Finally, l, which is a weighting factor for the vector element of tumor motion, is calculated as the fraction of the distance from the tumor and the distance from the nearest boundary of the thoracic cage.

A software application was developed to assess the motion of observation points based on orthogonal fluoroscopic imaging, compute a transformation map, and create a 3D-CT set for an arbitrary breathing phase. When creating a 3D-CT set using the 3D+ algorithm, manual work is required only to indicate the rough region of each observation point on fluoroscopic images and to select phase divisions and their positions. Subsequently, this software automatically assesses the motion of observation points. Specifically, the tumor position is tracked via pattern-matching techniques. The manually specified tumor region on one fluoroscopic image is set as a template pattern image, and the software detects the tumor position on other fluoroscopic images by searching for a similar pattern around a specified position. The chest wall and diaphragm motions are tracked via edge-detection techniques. The edges of the diaphragm and chest wall are easy to determine through image binarization because of the high contrast between the lungs and diaphragm or chest wall. After extracting boundary points between the lungs and chest wall or diaphragm, the robust Lowess smoothing method was applied to these boundary points to reduce the influence of image noise. In the present study, a smoothing span of 11 data points (about 5.0 mm) was used for this procedure.

II.C. Validation experiments

The geometrical accuracy of the 3D+ algorithm used to create 3D-CT data for an arbitrary phase from a known phase was evaluated by visual assessment, landmark analysis, and comparisons of the radial distance from the tumor centroid to the body or lung surface.

II.C.1. Patient data

To evaluate the accuracy of the 3D+ algorithm, we used 4D-CT data from eight patients with nonsmall cell lung cancer (NSCLC) who underwent stereotactic radiotherapy. CT data were acquired on a CT simulator (LightSpeed RT; General Electric Medical Systems, Waukesha, WI) in axial cine mode using a combined real-time position management system (RPM system, software version 1.6.5, Varian Medical Systems, Palo Alto, CA) for recording abdominal surface motion as a respiratory signal. Advantage 4D software (General Electric Medical Systems, Waukesha, WI) was used to create 4D-CT data sets. The slice thickness, field of view (FOV), and pixel size of each CT data set were 2.5, 520, and 1.0 mm, respectively.

Given that the end-exhale phase showed minimal motion artifacts or phase errors, CT data obtained in this phase were used as reference data. The CT data set for the end-inhale phase was created from acquired 3D-CT for the end-exhale phase using the 3D+ algorithm, and it was compared with the same phase data set obtained via 4D-CT. To eliminate differences in respiratory pattern during 4D-CT versus fluoroscopy, DRRs from 4D-CT were used to assess the displacement of observation points during the creation of the 3D-CT data set. In this case, the grid size for calculating the transformation vector was set to the same value as the CT pixel size (1.0 mm), and nearest-neighbor interpolation was used to reconstruct virtual CT sets.

II.C.2. Visual assessment

To evaluate the agreement of images obtained via 4D-CT versus the 3D+ algorithm, subtraction images derived from actual 4D-CT versus virtual 4D-CT were analyzed during the end-inhale phase. These subtraction images were visually inspected to compare the anatomical boundaries of the external body contour, lungs, heart, bones, spinal cord, and tumor.

II.C.3. Landmark analysis

Twenty vessel bifurcations inside the lung in the end-exhale CT images and their corresponding points in end-inhale CT images were identified as anatomical landmarks by an experienced radiation oncologist. All landmarks were selected within the diseased side of the lung in each patient. An example of landmarks identified in an end-exhale image from a representative patient is shown in Fig. 5. Based on the transformation map, the patient's landmarks were relocated in the end-inhale image and their coordinates compared with actual coordinates.

II.C.4. Comparison of radial distance

Errors in radial distance in virtual CT images created using the 3D+ algorithm are problematic because they could affect computed dose distribution. Therefore, the radial dis-

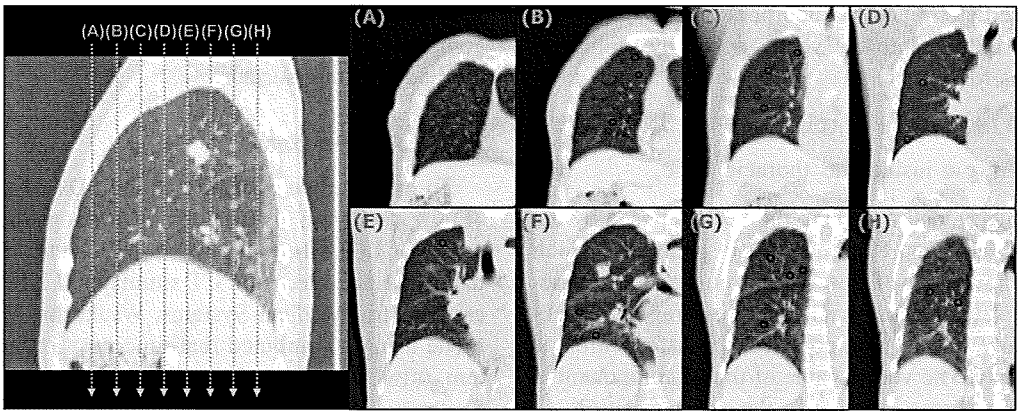

FIG. 5. Locations of anatomical landmarks selected for patient 1. Twenty vessel bifurcations were identified within the diseased side of the lung in an end-exhale CT image by an experienced radiation oncologist.

tances from the isocenter, which was set on the tumor centroid in the end-exhale image, to the body or lung surface were compared between the actual and created images for the end-inhale phase.

III. RESULTS

III.A. Displacement of observation points

The displacement values of observation points in the DRR images due to respiratory motion are summarized in Table I. These values were used to generate the transformation map and transformation vectors for each point. Although major displacements were observed on the surface of the dorsal diaphragm (range of 13–50 mm), ventral diaphragm movements were almost stable.

III.B. Computation time

In the validation experiments, the 3D+ application was run on a personal computer equipped with 3.4 GHz Pentium 4 processor. The computation time required to analyze fluoroscopic images was 0.514 s per frame, most of which was spent on pattern matching to detect tumor position. The computation time to create a virtual 4D-CT for an arbitrary phase using the 3D+ algorithm depended on the region of acquisition and image resolution. However, even the most complicated case in this study required only 40.6 s to create a 3D-CT data set, which consisted of a 512×512 matrix and 124 slices, for one phase. In addition to the automated computation time, using the 3D+ algorithm also involves some manual work, such as indicating the approximate region of the observation points and selecting the phase division, but the time required for this work is negligible.

III.C. Validation experiments

III.C.1. Visual assessment

Subtraction images derived from created versus actual CT images are shown in Fig. 6; the worst- and best-case scenarios are shown. The upper row shows subtraction images obtained by subtracting end-exhale 4D-CT images from end-inhale virtual CT images. End-inhale virtual CT images were created by deforming the end-exhale 4D-CT images according to the estimated transformation from the 3D+ algorithm. These subtraction images represent the degree of deformation using the 3D+ algorithm. The lower row shows the image comparison between virtual and actual CT images by subtracting the end-inhale actual 4D-CT images from the end-inhale virtual CT images. Moreover, to represent a full view of deformation based on the 3D+ algorithm, 3D

TABLE I. The displacement of observation points (mm) between the end-inhale and end-exhale (reference) phases were measured on DRRs produced using CT data from each phase. A positive value indicates that the observation point moves in the direction of lung expansion.

		Tumor motion (mm)			Chest wall motion (mm)		Diaphragm motion (in the SI direction) (mm)			
Patient No.	Tumor location	RL	AP	SI	RL	AP	Ventral	Top	Dorsal	Top of left diaphragm
1	Right lower	0	0	3	2	8	2	18	50	–
2	Right lower	0	0	12	0	1	0	15	18	–
3	Left upper	0	3	6	0	1	1	8	14	11
4	Right upper	0	2	3	1	1	0	9	17	–
5	Right upper	0	−3	0	0	2	0	10	13	–
6	Right upper	0	−2	0	1	2	0	21	27	–
7	Left lower	0	0	2	0	1	0	15	13	15
8	Right middle	−1	2	7	0	1	1	12	16	–

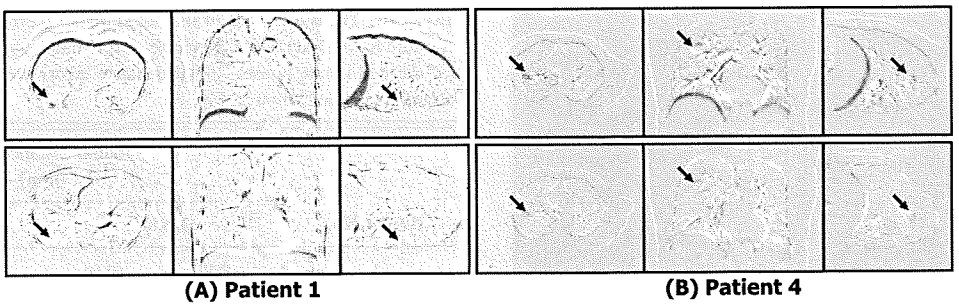

FIG. 6. Visual evaluation of virtual CT images created using the 3D+ algorithm for the worst (patient 1) and best cases (patient 4). The upper row shows subtraction images obtained by subtracting end-exhale 4D-CT images from end-inhale virtual CT images, whereas the lower row shows the subtraction of virtual CT versus actual 4D-CT images in the end-inhale phase. Arrows indicate tumor position. The gray region represents the area in which the densities of the two images are in good agreement, whereas the white/black region represents a region of disagreement.

surface-rendering images of bones and lungs from the same patients are shown in Fig. 7. The contours of the bones and lungs were extracted by binarization under the same threshold on each image. A discrepancy was observed around the heart region in patient 1 (A) because there was no adjustment for heart deformation caused by heartbeat and breathing motions in the 3D+ algorithm. Remarkably good agreement was observed in patient 4 (B).

III.C.2. Landmark analysis

Twenty landmarks (i.e., vessel bifurcations) were identified in the diseased lung in each patient. However, the accuracy of landmark identification was limited by the voxel size of $1.0\times1.0\times2.5$ mm^3. The mean distances [±standard deviation (SD)] between the predicted and actual landmarks are summarized in Table II. The averaged deviations for all landmarks ($n=160$) in the RL, AP, and SI directions and the 3D distance were 0.9, 1.4, 1.7, and 2.8 mm, respectively. As CT resolution was poor in the SI direction, deviations in the SI direction were larger than those in other directions. A systematic error in the RL direction was observed only for patient 1, who suffered from emphysema.

III.C.3. Comparison of radial distance

Maps showing the error in radial distance from the tumor centroid to the body and lung surfaces (virtual versus actual 4D-CT) for the patient presented in Fig. 6 are shown in Fig. 8 (worst and best cases). The region of directions in which a given ray passed through the top and bottom planes of the CT image is blacked out (invalid values). The area corresponding to the heart (left direction) and diaphragm (inferior direction) border caused larger deviation; however, beams that pass through these regions are not normally used from a clinical perspective (owing to the limited range of gantry/couch movement). A dotted rectangle (corresponding to the green-shaded area in the 3D view) was used to indicate the area through which clinically available beams pass. The mean radial distance errors (±SD) in this area are shown in Table III. The radial distance errors for the body and lung surface were almost within 1.0 and 2.0 mm, respectively.

IV. DISCUSSION

We developed an algorithm, designated 3D+, to simulate organ movement and deformation for 4D dose calculation. This 3D+ algorithm virtually creates continuous moving CT data sets, or "virtual 4D-CT," from static 3D-CT data and

TABLE II. The average and standard deviation (mm) between the predicted and actual coordinates of anatomical landmarks ($n=20$) in each direction and the 3D distance.

	Average (SD) deviation of landmark coordinates (mm)							
Patient No.	RL		AP		SI		3D distance	
1	2.7	(2.9)	2.6	(1.9)	2.9	(1.7)	5.4	(2.7)
2	0.7	(0.7)	1.2	(0.8)	0.9	(1.1)	2.0	(1.0)
3	0.4	(0.5)	1.6	(1.2)	2.7	(1.5)	3.4	(1.5)
4	0.5	(0.6)	0.7	(0.6)	1.0	(0.6)	1.5	(0.7)
5	0.6	(0.6)	1.7	(1.0)	1.3	(1.0)	2.5	(0.9)
6	1.1	(0.8)	1.2	(1.3)	1.7	(1.7)	2.9	(1.6)
7	0.4	(0.5)	1.0	(0.8)	1.7	(0.8)	2.2	(0.9)
8	0.6	(0.5)	1.1	(0.8)	1.1	(1.1)	1.9	(1.1)
All landmarks ($n=160$)	0.9	(1.4)	1.4	(1.2)	1.7	(1.4)	2.8	(1.8)

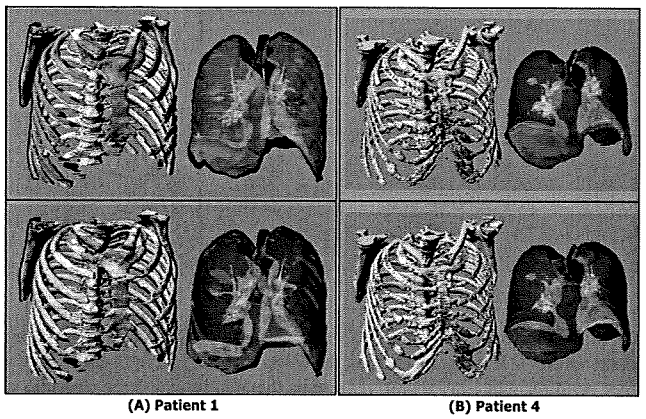

FIG. 7. Visual evaluation of virtual CT images created using the 3D+ algorithm with respect to bones and lungs, by 3D surface-rendering images for the worse (patient 1) and best (patient 4) cases. The upper row compares the end-exhale 4D-CT and end-inhale virtual CT images; the lower row compares the actual 4D-CT and virtual CT images at end-inhale. Red regions indicate areas of structural mismatch between the two images.

TABLE III. The mean ± SD of the radial distance error (mm) from the tumor centroid to the body and lung surfaces in virtual versus actual 4D-CT images for the end-inhale phase. Radial distance errors were estimated within the dotted rectangle shown in Fig. 8.

	Radial distance error (mm)			
Patient No.	Body		Lung	
1	−0.8	(2.0)	0.3	(2.3)
2	−0.2	(0.6)	−0.1	(3.0)
3	−0.4	(0.8)	−0.1	(1.5)
4	−0.5	(0.8)	−0.4	(0.9)
5	0.4	(1.1)	0.4	(1.3)
6	−0.1	(1.0)	1.6	(1.4)
7	0.1	(0.4)	−0.5	(1.6)
8	−0.4	(0.6)	−1.3	(1.3)

motion data at multiple observation points assessed by fluoroscopy. The insufficiency in motion data for generating a 4D model can be compensated for by adopting a typical motion model to collectively define common movements and deformations. The virtual 4D-CT was thus created by deforming the 3D-CT according to the typical motion model, in which patient-specific motion parameters measured via fluoroscopy were used.

The accuracy of the 3D+ algorithm is determined by the formulation of the typical motion model and selection of observation points. Several previous studies have used 4D-CT (Refs. 7, 8, and 25–27) and magnetic resonance imaging[28,29] to analyze and characterize respiratory organ motion, and these data are useful in the configuration of a typical motion model and the determination of observation points. Observation points are typically set at multiple sites that will allow the characterization of movement and deformation (e.g., the diaphragm and chest wall). Moreover, observation points in the tumor should be defined individually because tumor motion does not always correlate with its anatomical location, size, or pulmonary function.[30,31] For instance, a tumor in the lower lobe attached to the chest wall did not exhibit movement even when the diaphragm moved dynamically. In this study, 4D-CT and fluoroscopic image data for patients with discernible lung tumors were used to evaluate accuracy of the 3D+ algorithm, but it is often difficult or impossible to discern the tumor under fluoroscopy. Fluoroscopic imaging from other angles can be used to visualize these difficult tumors, or it may be necessary to track the motion of any other discernible structure near the tumor, such as an implantable fiducial marker.[32–34] It is also important to acquire artifact-free 3D-CT data when using the 3D + algorithm, because any artifact in the original 3D-CT will be inherited by all subsequent CT images. In general, if the breathing period for the exhale phase is relatively longer than that for the inhale phase, then the position of the tumor is most stable and reproducible during the exhale phase.[35,36] Therefore, the exhale phase is more likely to provide artifact-free 3D-CT data.

The geometric accuracy of virtual CT images created us-

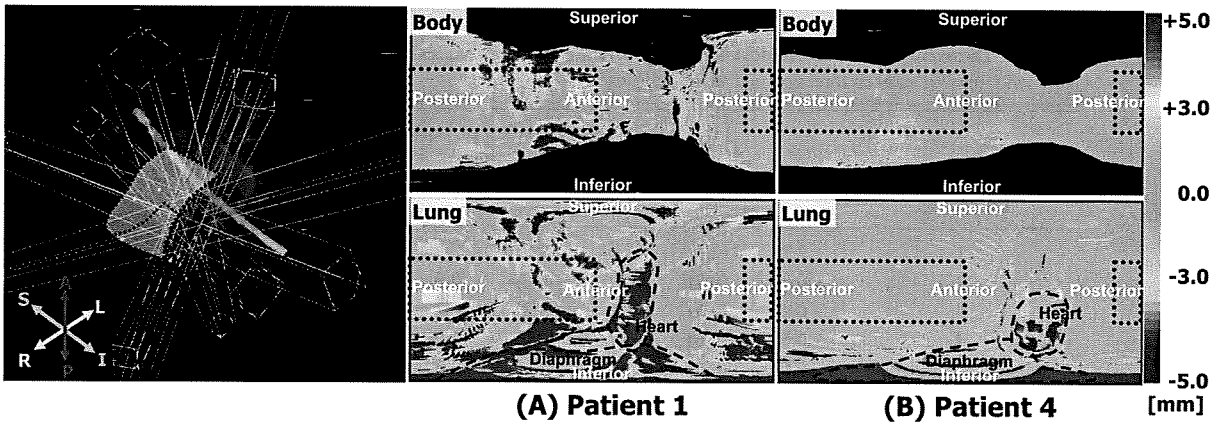

FIG. 8. Maps showing the error in radial distance from the tumor centroid to the body (upper) and lung (lower) surfaces for virtual versus actual 4D-CT images. Regarding radial distance error for the body, the region of directions in which a given ray passed through the top and bottom plane of CT images is blacked out (invalid values). A dotted rectangle (green-shaded area in the 3D view) indicates the area through which clinically available beams pass.

ing the 3D+ algorithm was validated by comparing them to actual 4D-CT images. They showed a mean accuracy of 2.8 ± 1.8 mm for all patients, as determined by landmark analysis, which is very similar to values obtained in previous studies using 4D-CT and deformable image registration.[17–19,37,38] For example, Sarrut *et al.* (2006) reported a value of 2.7 ± 1.1 mm,[17] and Rietzel and Chen (2006) reported a value of 2.1 ± 1.5 mm.[37] Systematic error was observed in one patient suffering from emphysema (Table II, patient 1), which probably occurred because emphysematous regions lose elasticity and move differently than the normal lung, making it difficult to distinguish movement via fluoroscopy in these regions. These results suggest that pre-existing lung disease, such as emphysema, bulla, or fibrosis, may reduce the geometrical accuracy of virtual 4D-CT images created using the 3D+ algorithm.

The radial distance from the tumor centroid to the body and lung surfaces showed very little variation in virtual versus actual 4D-CT images. For a 6 MV x-ray field, these minimal variations in the chest wall depth and lung thickness produced a computational error of $<2\%$ in the absorbed dose at the isocenter, as estimated using a commercial treatment planning system with a superposition algorithm for dose calculation. Therefore, the difference in path length for almost all beams would have only negligible effects on dose calculation. These results suggest that the accuracy of dose distributions calculated based on virtual 4D-CT images may be clinically acceptable, except within the mediastinal region, where geometrical errors often occur due to peristalsis, cardiac motion, and aortic pulsation.[31,39]

The 3D+ algorithm was designed for ease of clinical use and computation efficiency rather than rigorous accuracy. Therefore, the typical motion model was constructed such that the transformation vectors could be determined using linear equations alone, and the observation points were pared to the minimum. This simplified model may result in the creation of unrealistic deformations, such as the expanding or shrinking volume of the heart, aorta, bronchus, and chest wall. If a nonlinear viscoelastic model based on respiratory system mechanics is incorporated into this algorithm, more realistic and accurate models may be achieved. Additional data, such as the position of external markers on the patient's chest or abdomen or the shape of the body surface measured using an infrared device[40,41] or optical scanner,[42,43] would be helpful to complement the motion data described here and would further improve the accuracy of the 3D+ algorithm. Thus, although the accuracy of the current 3D+ algorithm is acceptable for clinical use, further improvements are possible.

Although organ motion can be quantified exactly via 4D-CT, three types of errors should be addressed by the current commercially available 4D-CT system that uses a cine scanning protocol and retrospective image reconstruction: A residual motion artifact,[8,44] the phase difference between the motion of an internal target and an external marker for a respiratory signal,[31,45] and reconstruction artifacts due to phase variation.[8–10] Because a regular respiratory pattern is not achievable in all patients, it is likely that respiratory conditions, such as the trajectory and amplitude of respiratory motion and respiratory rate, change in each slice of the 4D-CT.[32,36,46,47] Furthermore, 4D-CT involves substantial processing times associated with image reconstruction and deformable image registration. Deformable image registration, in particular, is a computationally intensive task, with a typical execution time on the order of minutes on most modern desktop computers.[17–20] In addition, even when 4D-CT data sets are available, it is impossible to perfectly simulate future movements and deformations[48] because 4D-CT can only show past data.

On the other hand, the 3D+ algorithm can theoretically be used for all selected observation points where motion data are measurable, but it is basically confined to a limited area. For diseases such as lung tumors, where the motion of the target and surrounding structures can be easily assessed via fluoroscopy, the 3D+ algorithm may be applicable. The 3D + algorithm may also be useful for organs in the upper abdomen, such as the liver, that move significantly with respiration.[25,26] However, even for these sites, virtual 4D-CT created using the 3D+ algorithm may show geometrically systematic errors in all regions except for that defined by the observation points, because their transformation vectors are determined by calculation and interpolation based on the typical motion model. In the case of tumors close to OARs, such as the heart, aorta, and trachea, the adequacy of virtual 4D-CT should be reviewed. Although the 3D+ algorithm does possess these limitations, it is a clinically reasonable approach because the typical motion pattern, observed via fluoroscopic imaging, is taken into consideration. In addition, it is not hindered by phase variation in each slice, as is virtual 4D-CT. In terms of computation time, the 3D+ algorithm is more suitable for routine clinical use than 4D-CT and deformable image registrations. The 3D+ algorithm, which does not require deformable image registration, can provide virtual 4D-CT images in a few minutes, and it may be possible to further reduce computation time. For instance, analyzing the motion of observation points can be executed concurrently with fluorography. Regarding the creation of virtual 4D-CT images, it is not always necessary to reconstruct entire 3D-CT images, so it may be possible to reduce computation time by limiting reconstruction to the diseased side of the body.

Furthermore, the 3D+ algorithm can be easily applied to 4D dose calculation and would be useful for adaptive radiation therapy. If motion data for observation points are assessed during irradiation via online kilovoltage fluoroscopy,[33,49] daily dose distribution can be estimated by utilizing the 3D+ algorithm without acquiring additional CT images. The dose discrepancy between the planned and accumulated daily delivered doses may be corrected by applying an adaptive feedback correction for the next irradiation. Thus, the 3D+ algorithm has great potential in terms of adaptive radiation therapy.

V. CONCLUSION

This study describes the development of a new algorithm, designated 3D+, to simulate organ movement and deforma-

tion for 4D dose calculation. The 3D+ algorithm creates virtual 4D-CT images from a static 3D-CT and motion data at multiple observation points assessed via fluoroscopy. The accuracy of these virtual 4D-CT images was evaluated by comparing them to actual 4D-CT images. These validation experiments indicated that the 3D+ algorithm produces similar results to 4D-CT and deformable image registration for sites such as the lung, where organ movement can be easily assessed by fluoroscopy. The 3D+ algorithm is also suitable for routine clinical use in terms of the processing time and amount of data processed. In addition, the 3D+ algorithm will be useful for 4D dose calculation for advanced beam delivery techniques, such as real-time tumor tracking irradiation and adaptive radiation therapy.

ACKNOWLEDGMENTS

This study was supported in part by a Grant for the Practical Application of Next-Generation Strategic Technology by the New Energy and Industrial Technology Development Organization (Grant No. 0901102, 2007), a Grant-in-Aid for Scientific Research on Priority Areas (Cancer) from the Ministry of Education, Culture, Sports, Science, and Technology of Japan (Grant No. 17016036), and Grants-in-Aid for Scientific Research from the Ministry of Education, Culture, Sports, Science, and Technology of Japan (Grant Nos. 17390333 and 20229009). The subject of this research is protected under a Japanese Patent Application (No. 2007-317653).

[a]Electronic mail: miyabe@kuhp.kyoto-u.ac.jp

[1]P. J. Keall *et al.*, "The management of respiratory motion in radiation oncology," Report of AAPM Task Group 76, 2006.
[2]H. Shirato, Y. Seppenwoolde, K. Kitamura, R. Onimura, and S. Shimizu, "Intrafractional tumor motion: Lung and liver," Semin. Radiat. Oncol. **14**, 10–18 (2004).
[3]K. M. Langen and D. T. L. Jones, "Organ motion and its management," Int. J. Radiat. Oncol., Biol., Phys. **50**, 265–278 (2001).
[4]G. T. Y. Chen, J. H. Kung, and K. P. Beaudette, "Artifacts in computed tomography scanning of moving objects," Semin. Radiat. Oncol. **14**, 19–26 (2004).
[5]International Commission on Radiation Units and Measurements, "Prescribing, recording and reporting photon beam therapy (supplement to ICRU Report 50)," ICRU Report No. 62, 1999.
[6]M. Schwarz, J. V. Geer, M. V. Hark, J. V. Lebesque, B. J. Mijnheer, and E. M. F. Damen, "Impact to geometrical uncertainties on 3D CRT and IMRT dose distributions for lung cancer treatment," Int. J. Radiat. Oncol., Biol., Phys. **65**, 1260–1269 (2006).
[7]G. S. Mageras, A. Pevsner, E. D. Yorke, K. E. Rosenzweig, E. C. Ford, A. Hertanto, S. M. Larson, D. M. Lovelock, Y. E. Erdi, S. A. Nehmeh, J. L. Humm, and C. C. Ling, "Measurement of lung tumor motion using respiration-correlated CT," Int. J. Radiat. Oncol., Biol., Phys. **60**, 933–941 (2004).
[8]D. A. Low, M. Nystrom, E. Kalinin, P. Parikh, J. F. Dempsey, J. D. Bradley, S. Mutic, S. H. Wahab, T. Islam, G. Christensen, D. G. Politte, and R. Whiting, "A method for the reconstruction of four-dimensional synchronized CT scans acquired during free breathing," Med. Phys. **30**, 1254–1263 (2003).
[9]E. Rietzel, T. Pan, and G. T. Y. Chen, "Four-dimensional computed tomography: Image formation and clinical protocol," Med. Phys. **32**, 874–889 (2005).
[10]T. Pan, T. Lee, E. Rietzel, and G. T. Y. Chen, "4D-CT imaging of a volume influenced by respiratory motion on multi-slice CT," Med. Phys. **31**, 333–340 (2004).
[11]S. Gao, L. Zhang, H. Wang, R. D. Crevoisir, D. D. Kuban, R. Mohan, and L. Dong, "A deformable image registration method to handle distended rectums in prostate cancer radiotherapy," Med. Phys. **33**, 3304–3312 (2006).
[12]J. P. W. Pluim, J. B. A. Maints, and M. A. Viergever, "Mutual-information-based registration of medical images: A survey," IEEE Trans. Med. Imaging **22**, 986–1004 (2003).
[13]K. K. Brock, M. B. Sharpe, L. A. Dawson, S. M. Kim, and D. A. Jaffray, "Accuracy of finite element model-based multi-organ deformable image registration," Med. Phys. **32**, 1647–1659 (2005).
[14]P. Keall, "4-dimensional computed tomography imaging and treatment planning," Semin. Radiat. Oncol. **14**, 81–90 (2004).
[15]E. Rietzel, G. T. Y. Chen, N. C. Choi, and C. G. Willet, "Four-dimensional image-based treatment planning: Target volume segmentation and dose calculation in the presence of respiratory motion," Int. J. Radiat. Oncol., Biol., Phys. **61**, 1535–1550 (2005).
[16]P. J. Keall, S. Joshi, S. S. Vedam, J. V. Siebers, V. R. Kini, and R. Mohan, "Four-dimensional radiotherapy planning for DMLC-based respiratory motion tracking," Med. Phys. **32**, 942–951 (2005).
[17]D. Sarrut, V. Boldea, S. Miguet, and C. Ginestet, "Simulation of four-dimensional CT images from deformable registration between inhale and exhale breath-hold CT scans," Med. Phys. **33**, 605–617 (2006).
[18]K. M. Brock, J. M. Balter, L. A. Dawson, M. L. Kessler, and C. R. Meyer, "Automated generation of a four-dimensional model of the liver using warping and mutual information," Med. Phys. **30**, 1128–1133 (2003).
[19]A. Pevsner, B. Davis, S. Joshi, A. Hertanto, J. Mechalakos, E. Yorke, K. Rosenzweig, S. Nehmeh, Y. E. Erdi, J. L. Humm, S. Larson, C. C. Ling, and G. S. Mageras, "Evaluation of an automated deformable image matching method for quantifying lung motion in respiration-correlated CT images," Med. Phys. **33**, 369–376 (2006).
[20]T. Rohlfing and C. R. Maurer, "Nonrigid image registration in shared-memory multiprocessor environments with application to brains, breasts, and bees," IEEE Trans. Inf. Technol. Biomed. **7**, 16–25 (2003).
[21]M. D. Goldman and J. Mead, "Mechanical interaction between the diaphragm and rib cage," J. Appl. Physiol. **35**, 197–204 (1973).
[22]T. J. Hixon and J. D. Hoit, "Physical examination of the rib cage wall by the speech-language pathologist," Am. J. Speech Lang. Pathol. **9**, 179–196 (2000).
[23]P. Giraud, Y. D. Rycke, B. Dubray, S. Helfre, D. Voican, L. Guo, J. Rosenwald, K. Keraudy, M. Housset, E. Touboul, and J. Cosset, "Conformal radiotherapy (CRT) planning for lung cancer: Analysis of intrathoracic organ motion during extreme phases of breathing," Int. J. Radiat. Oncol., Biol., Phys. **51**, 1081–1092 (2001).
[24]International Commission on Radiation Units and Measurements, "Use of computers in external beam radiotherapy procedures with high energy photons and electrons," ICRU Report No. 42, 1987.
[25]A. S. Beddar, K. Kainz, T. M. Briere, Y. Tsunashima, T. Pan, K. Prado, R. Mohan, M. Gillin, and S. Krishnan, "Correlation between internal fiducial tumor motion and external marker motion for liver tumors imaged with 4D-CT," Int. J. Radiat. Oncol., Biol., Phys. **67**, 630–638 (2007).
[26]E. D. Brandner, A. Wu, H. Chen, D. Heron, S. Kalnicki, K. Komanduri, K. Gerszten, S. Burton, I. Ahmed, and Z. Shou, "Abdominal organ motion measured using 4D CT," Int. J. Radiat. Oncol., Biol., Phys. **65**, 554–560 (2006).
[27]E. M. T. Dieleman, S. Senan, A. Vincent, F. J. Lagerwaard, B. J. Slotman, and J. R. van Sörnsen de Koste, "Four-dimensional computed tomographic analysis of esophageal mobility during normal respiration," Int. J. Radiat. Oncol., Biol., Phys. **67**, 775–780 (2007).
[28]C. Plathow, S. Ley, C. Fink, M. Puderbach, W. Hosch, A. Schmähl, J. Debus, and H. Kauczor, "Analysis of interthoracic tumor mobility during whole breathing cycle by dynamic MRI," Int. J. Radiat. Oncol., Biol., Phys. **59**, 952–959 (2004).
[29]J. M. Blackall, S. Ahmad, M. E. Miquel, J. R. McClelland, D. B. Landau, and D. J. Hawkes, "MRI-based measurements of respiratory motion variability and assessment of imaging strategies for radiotherapy planning," Phys. Med. Biol. **51**, 4147–4169 (2006).
[30]C. W. Stevens, R. F. Munden, K. M. Forster, J. F. Kelly, Z. Liao, G. Starkschall, S. Tucker, and R. Komaki, "Respiratory-driven lung tumor motion is independent of tumor size, tumor location, and pulmonary function," Int. J. Radiat. Oncol., Biol., Phys. **51**, 62–68 (2001).
[31]Y. Seppenwoolde, H. Shirato, K. Kitamura, S. Shimizu, M. V. Herk, J. V. Lebesque, and K. Miyasaka, "Precise and real-time measurement of 3D tumor motion in lung due to breathing and heartbeat, measured during radiotherapy," Int. J. Radiat. Oncol., Biol., Phys. **53**, 822–834 (2002).

[32]C. Ozhasoglu and M. J. Murphy, "Issues in respiratory motion compensation during external-beam radiotherapy," Int. J. Radiat. Oncol., Biol., Phys. **52**, 1389–1399 (2002).
[33]H. Shirato, S. Shimizu, T. Kunieda, K. Kitamura, M. van Herk, K. Kagei, T. Nishioka, S. Hashimoto, K. Fujita, H. Aoyama, K. Tsuchiya, K. Kudo, and K. Miyasaka, "Physical aspects of a real-time tumor-tracking system for gated radiotherapy," Int. J. Radiat. Oncol., Biol., Phys. **48**, 1187–1195 (2000).
[34]J. M. Balter, L. A. Dawson, S. Kazanjian, C. McGinn, K. K. Brack, T. Lawrence, and R. Ten Haken, "Determination of ventilatory liver movement via radiographic evaluation of diaphragm position," Int. J. Radiat. Oncol., Biol., Phys. **51**, 267–270 (2001).
[35]J. M. Balter, K. L. Lam, C. J. McGinn, T. S. Lawrence, and R. K. Ten Haken, "Improvement of CT-based treatment-planning models of abdominal targets using static exhale imaging," Int. J. Radiat. Oncol., Biol., Phys. **41**, 939–943 (1998).
[36]H. Wu, G. C. Sharp, Q. Zhao, H. Shirato, and S. B. Jiang, "Statistical analysis and correlation discovery of tumor respiratory motion," Phys. Med. Biol. **52**, 4761–4774 (2007).
[37]E. Rietzel and G. T. Y. Chen, "Deformable registration of 4D computed tomography data," Med. Phys. **33**, 4423–4430 (2006).
[38]M. M. Coselmon, J. M. Balter, D. L. McShan, and M. L. Kessler, "Mutual information based CT registration of the lung at exhale and inhale breathing states using thin-plate splines," Med. Phys. **31**, 2942–2948 (2004).
[39]L. Ekberg, O. Holmberg, L. Wittgren, G. Bjelkengren, and T. Landberg, "What margins should be added to the clinical target volume in radiotherapy treatment planning for lung cancer?," Radiother. Oncol. **48**, 71–77 (1998).
[40]H. Liu, Y. Yu, M. C. Schell, W. G. O'Dell, R. Ruo, and P. Okunieff, "Optimal marker placement in photogrammetry patient positioning system," Med. Phys. **30**, 103–110 (2003).
[41]I. Frosio, M. Spadea, E. De Momi, M. Ridoldi, G. Baroni, G. Ferrigno, R. Orecchia, and A. Pedotti, "A neural network based method for optical patient set-up registration in breast radiotherapy," Ann. Biomed. Eng. **34**, 677–686 (2006).
[42]L. Kovacs, A. Zimmermann, G. Brockmann, M. Gühring, H. Baurecht, N. A. Papadopulus, K. Schwenzer-Zimmerer, R. Sader, E. Biemer, and H. F. Zeilhofer, "Three-dimensional recording of the human face with a 3D laser scanner," J. Plast. Reconstr. Aesthet. Surg. **59**, 1193–1202 (2006).
[43]L. Kovacs, A. Zimmermann, G. Brockmann, H. Baurecht, K. Schwenzer-Zimmerer, N. A. Papadopulus, M. A. Papadopoulos, R. Sader, E. Biemer, and H. F. Zeilhofer, "Accuracy and precision of the three-dimensional assessment of the facial surface using a 3-D laser scanner," IEEE Trans. Med. Imaging **25**, 742–754 (2006).
[44]S. S. Vedam, P. J. Keall, V. R. Kini, H. Mostafavi, H. P. Shukla, and R. Mohan, "Acquiring a four-dimensional computed tomography dataset using an external respiratory signal," Phys. Med. Biol. **48**, 45–62 (2003).
[45]G. S. Mageras, E. Yorke, K. Rosenzweig, L. Braban, E. Keatly, E. Ford, S. A. Leibel, and C. C. Ling, "Fluoroscopic evaluation of diaphragmatic motion reduction with a respiratory gated radiotherapy system," J. Appl. Clin. Med. Phys. **2**, 191–200 (2001).
[46]J. Cai, P. W. Read, T. A. Altes, J. A. Molloy, J. R. Brookenman, and K. Sheng, "Evaluation of the reproducibility of lung motion probability distribution function (PDF) using dynamic MRI," Phys. Med. Biol. **52**, 365–373 (2007).
[47]H. Shirato, K. Suzuki, G. C. Sharp, K. Fujita, R. Onimaru, M. Fujino, N. Kato, Y. Osaka, R. Kinoshita, H. Taguchi, S. Onodera, and K. Miyasaka, "Speed and amplitude of lung tumor motion precisely detected in four-dimensional setup and in real-time tumor-tracking radiotherapy," Int. J. Radiat. Oncol., Biol., Phys. **64**, 1229–1236 (2006).
[48]G. Hugo, C. Vargas, J. Liang, L. Kestin, J. W. Wong, and D. Yan, "Changes in the respiratory pattern during radiotherapy for cancer in the lung," Radiother. Oncol. **78**, 326–331 (2006).
[49]Y. Kamino, K. Takayama, M. Kokubo, Y. Narita, E. Hirai, N. Kawada, T. Mizowaki, Y. Nagata, T. Nishidai, and M. Hiraoka, "Development of a four-dimensional image-guided radiotherapy system with a gimbaled x-ray head," Int. J. Radiat. Oncol., Biol., Phys. **66**, 271–278 (2006).

Int. J. Radiation Oncology Biol. Phys., Vol. 75, No. 2, pp. 558–563, 2009

0360-3016/09/$–see front matter

ELSEVIER

doi:10.1016/j.ijrobp.2008.11.070

5TH JUCTS AND THE 5TH S. TAKAHASHI MEMORIAL INTERNATIONAL JOINT SYMPOSIUM

EFFECT OF AUDIO COACHING ON CORRELATION OF ABDOMINAL DISPLACEMENT WITH LUNG TUMOR MOTION

MITSUHIRO NAKAMURA, M.S.,* YUICHIRO NARITA, PH.D.,* YUKINORI MATSUO, M.D., PH.D.,* MASARU NARABAYASHI, M.D.,* MANABU NAKATA, R.T.T.,† AKIRA SAWADA, PH.D.,* TAKASHI MIZOWAKI, M.D., PH.D.,* YASUSHI NAGATA, M.D., PH.D.,‡ AND MASAHIRO HIRAOKA, M.D., PH.D.*

*Department of Radiation Oncology and Image-applied Therapy, Kyoto University Graduate School of Medicine, Kyoto, Japan; †Clinical Radiology Service Division, Kyoto University Hospital, Kyoto, Japan; and ‡Division of Radiation Oncology, Hiroshima University Hospital, Hiroshima, Japan

Purpose: To assess the effect of audio coaching on the time-dependent behavior of the correlation between abdominal motion and lung tumor motion and the corresponding lung tumor position mismatches.

Methods and Materials: Six patients who had a lung tumor with a motion range >8 mm were enrolled in the present study. Breathing-synchronized fluoroscopy was performed initially without audio coaching, followed by fluoroscopy with recorded audio coaching for multiple days. Two different measurements, anteroposterior abdominal displacement using the real-time positioning management system and superoinferior (SI) lung tumor motion by X-ray fluoroscopy, were performed simultaneously. Their sequential images were recorded using one display system. The lung tumor position was automatically detected with a template matching technique. The relationship between the abdominal and lung tumor motion was analyzed with and without audio coaching.

Results: The mean SI tumor displacement was 10.4 mm without audio coaching and increased to 23.0 mm with audio coaching ($p < .01$). The correlation coefficients ranged from 0.89 to 0.97 with free breathing. Applying audio coaching, the correlation coefficients improved significantly (range, 0.93–0.99; $p < .01$), and the SI lung tumor position mismatches became larger in 75% of all sessions.

Conclusion: Audio coaching served to increase the degree of correlation and make it more reproducible. In addition, the phase shifts between tumor motion and abdominal displacement were improved; however, all patients breathed more deeply, and the SI lung tumor position mismatches became slightly larger with audio coaching than without audio coaching. © 2009 Elsevier Inc.

Lung cancer, tumor motion, respiratory gated radiotherapy, audio coaching, correlation.

INTRODUCTION

During conventional radiotherapy (RT) planning for tumor movement with respiration, an internal margin is added around the clinical target volume to ensure complete coverage of the clinical target volume as it moves because of respiration within a treatment session (1). Therefore, it follows that a large amount of the surrounding normal tissue will be irradiated, increasing the amount of healthy tissue irradiated and limiting the maximal dose that can be prescribed to the tumor itself. An abdominal plate, called "diaphragm control (DC)," has been reported to be suitable for lung tumors to regulate respiratory motion (2). Although DC has been applied for patients during stereotactic body RT (SBRT) when the lung tumor motion was >8 mm at our institution, it was found that DC sometimes had little effect and was unusable because of poor respiratory function.

As techniques to explicitly account for respiratory-induced tumor movement, breath-hold (3–5), respiratory gated RT (6–10), and four-dimensional (11, 12) techniques are effective in reducing internal margin, resulting in a lower dose to the normal tissue and thus a lower risk of complications. Among these techniques, respiratory gated RT has been successfully applied to thorax and abdomen lesions in some institutions (6–10). During respiratory gated RT, the treatment device is periodically turned on and off, in phase or amplitude with the patient's breathing pattern, to restrict

Reprint requests to: Mitsuhiro Nakamura, M.S., Kyoto University Graduate School of Medicine, Kyoto, 54 Kawahara-cho, Shogoin, Sakyo-ku, Kyoto 606-8507 Japan. Tel: (+81) 75-751-3419; Fax: (+81) 75-771-9749; E-mail: m_nkmr@kuhp.kyoto-u.ac.jp

Supported in part by a Grant-in-Aid for Scientific Research from the Ministry of Education, Culture, Sports, Science and Technology of Japan (Grant 20229009).

Presented in part at the Fifth Japan-U.S. Cancer Therapy Symposium and the Fifth S. Takahashi Memorial International Joint Symposium, Sendai, Japan, September 7–9, 2007.

Conflict of interest: none.

Received Aug 27, 2008, and in revised form Nov 17, 2008. Accepted for publication Nov 22, 2008.

the range of tumor positions during dose delivery. Two types of gating methods have been categorized: internal and external gated RT. Internal gated RT accurately delivers a dose by monitoring the tumor position in real time using implanted fiducial markers (8). External gated RT requires the acquisition of a respiration surrogate signal to represent the tumor position (6, 7, 9, 10). Although external gated RT is less invasive for patients, the accuracy of the correlation depends on the stability of the tumor-surrogate phase or amplitude relationships during the treatment course.

In our institution, we are scheduled to perform external gated RT for patients who need DC during SBRT for lung cancer or advanced-stage lung cancer; however, we have been concerned about the correlation between the abdominal displacement and lung tumor motion in the superoinferior (SI) direction. Although Ahn *et al.* (13) and Hoisak *et al.* (14) reported a generally strong correlation without implanted fiducial markers, no guarantee exists that similar results have been obtained at our institution. Some researchers have also reported that the phase of organ motion does not necessarily match that of the surrogate motion (13–19). Phase shifts must be addressed to maintain the accuracy of the gating window. Ionascu *et al.* (17) used a real-time RT system and quantitatively estimated the time-dependent behavior of the correlation between abdominal displacement and implanted fiducial marker motion, and their corresponding amplitude mismatches. They suggested that it is necessary to increase the treatment margins to ensure the phase shifts.

The preliminary study for gated RT began under an institutional review board-approved protocol in May 2007. We developed an in-house method to investigate the tumor–abdominal motion relationship without implanted fiducial markers and showed a high correlation between these motions for 11 patients with lung cancer during free breathing (19). In addition, we have been planning to incorporate audio coaching to improve the efficiency of external gated RT for patients with an irregular breathing pattern (20, 21). Although Kini *et al.* (20) concluded that audio coaching improved the stability of respiration frequency, the effect of audio coaching on phase shifts and their corresponding lung tumor position mismatches have not yet been examined.

The purpose of the present study was to assess the effect of audio coaching on the correlations of abdominal displacement with lung tumor motion in the SI direction and the SI lung tumor position mismatches between abdominal displacement as a surrogate for the lung tumor position and the measured lung tumor position.

METHODS AND MATERIALS

Patients

Of the patients who underwent SBRT in four fractions for lung tumors between May 2007 and December 2007, 6 patients, who met following criteria, were enrolled in the present study: the lung tumor was clearly identified by X-ray fluoroscopy (Acuity, Varian Medical Systems, Palo Alto, CA) and the average peak-to-trough SI extent of the lung tumor displacement was >8 mm with X-ray fluoroscopy, as verified by several radiation oncologists. Of the 6 patients, 4 were men and 2 were women (median age, 78 years; range, 62–81). The lung tumors were located in the right middle lobe (n = 1), right lower lobe (n = 3), left upper lobe (n = 1), and left lower lobe (n = 1). The patient characteristics are listed in Table 1.

Data acquisition

A marker block with two infrared reflecting dots was placed on the anterior abdominal surface of the patient. The anteroposterior (AP) abdominal skin surface displacement was measured using the real-time positioning management system (Varian Medical Systems). The SI lung tumor motion was simultaneously acquired using X-ray fluoroscopy from the anterior of the patients. The X-ray fluoroscopy video signal was recorded at a frame rate of 30 Hz. The screen of the computer monitoring the abdominal displacement was displayed in parallel on the X-ray fluoroscopy console monitor using the remote desktop feature (maximal data transfer rate, 1 Gb/s) in Windows XP Professional so that the lung tumor motion and abdominal displacement were displayed on the same screen (Fig. 1). From the results of the preliminary verification, the phase error due to the signal delay of the local area network connection was sufficiently small (19).

All patients underwent an X-ray fluoroscopic examination of 60 s in duration with free breathing. They were then asked to breathe following simple audio coaching, such as "breathe in, breathe out," at a suitable tempo for each patient. They were trained for 5 min with the audio coaching to ensure they were comfortable with the breathing tempo and to make any adjustments necessary. After the breathing exercise, an X-ray fluoroscopic examination was performed again with audio coaching for 60 s. The X-ray fluoroscopy console monitor on which the abdominal displacement was simultaneously displayed was recorded on a digital video disk for each measurement. The measurements were performed at SBRT planning (Session 1), the second treatment session (Session 2), and at the end of treatment (Session 3). The interval between Sessions 1 and 3 was 10 days, and the duration of SBRT was within 1 week.

Tracking procedure and analysis

Custom software was developed by a medical physicist (M.N.) to automatically identify the lung tumor position to be detected on fluoroscopic images. The feasibility of our method for identifying the lung tumor position has been previously proved (19).

First, the software reads the recorded fluoroscopic images and runs the following procedure. A reflective marker position was detected using binary image processing and the mean AP abdominal displacement was then calculated. After measuring the reflective marker position, a rectangular region of interest (ROI) was set in the image that sufficiently contained the extent of lung tumor motion throughout the whole breathing cycle. A median filter with a 3 × 3 filter kernel was used to reduce the noise within the ROI. Image histograms within the ROI were equalized to enhance the contrast between the lung tumor and the background; thereafter, a template matching technique was applied to automatically detect the lung tumor. We have found that a basic single-template approach for lung tumor tracking does not work well for lung tumor tracking on X-ray fluoroscopic images because of the following tumor motion characteristics: the projected lung tumor shape and appearance vary more or less as a function of the breathing phase; and the X-ray fluoroscopic image intensities change with chest expansion and contraction. To reduce the false detection of the lung tumor position, three templates of the lung tumor for the exhale (end-ex), inhale

Table 1. Patient characteristics

Pt. No.	Age (y)	Gender	PS	Tumor location	Tumor size (mm)
1	78	Male	0	RLL	23
2	77	Male	1	RLL	20
3	62	Female	0	LLL	18
4	81	Male	0	LUL	29
5	77	Female	0	RLL	15
6	78	Male	0	RML	27

Abbreviations: Pt. No. = patient number; PS = performance status; RLL = right lower lobe; LLL = left lower lobe; LUL = left upper lobe; RML = right middle lobe.

(end-in), and middle (mid) respiratory phase were used. The method of difference measures ($D_k, k \in [end\text{-}in, end\text{-}ex, mid]$), based on the square of the difference between the templates and the background image, was defined as follows:

$$D_{end-in}(x,y) = \sum_{i=0}^{M-1}\sum_{j=0}^{N-1}\{f(x+i,y+j) - g_{end-in}(i,j)\}^2 \quad (1)$$

$$D_{end-ex}(x,y) = \sum_{i=0}^{M-1}\sum_{j=0}^{N-1}\{f(x+i,y+j) - g_{end-ex}(i,j)\}^2 \quad (2)$$

$$D_{mid}(x,y) = \sum_{i=0}^{M-1}\sum_{j=0}^{N-1}\{f(x+i,y+j) - g_{mid}(i,j)\}^2 \quad (3)$$

where N and M represent the length and width of the template, and $f(x, y)$ and $g_k(x, y)$, ($k \in [end\text{-}in, end\text{-}ex, mid]$) is the pixel intensity at location (x, y) of the ROI and templates, respectively. The region of minimal difference can be determined as the location of the lung tumor (x^*, y^*), as follows:

$$(x*, y*) = \arg\min_{(x,y)\in ROI}(D_{end-in}(x,y), D_{end-ex}(x,y), D_{mid}(x,y)) \quad (4)$$

The average displacement of lung tumor motion was measured according to the maximal peak-to-trough SI extent of the tumor displacement. To evaluate the tumor–abdominal phase relationship, the cross-correlation of the time-synchronized tumor–abdominal motion and its phase shifts was calculated. The SI lung tumor position mismatches between the predicted and measured lung tumor position were computed according to the method of Ionascu *et al.* (17). The mean value and 99% confidence interval of the SI lung tumor position mismatches were also calculated. The one-sided Wilcoxon test was performed for the statistical analyses. Values of $p < .01$ were regarded as significant.

RESULTS

Figure 2a,b illustrates the SI tumor displacement and AP abdominal displacement during the full respiratory cycle with and without audio coaching, respectively. The error bars represent the standard deviation (SD). The mean ± SD of tumor displacement was 10.4 ± 3.0 mm (range, 8.2–18.9) for patients during free breathing (FB). Audio coaching increased the displacement to a mean ± SD of 23.0 ± 11.6 mm (range, 10.1–46.2). The mean ± SD of abdominal displacement was 6.5 ± 2.2 mm for FB. These values increased to 17.3 ± 6.1 mm with audio coaching. A significant difference was observed between these groups in both displacements ($p < .01$).

Table 2 lists the correlation coefficients of tumor motion with abdominal displacement for each patient with and without audio coaching. The mean ± SD of the correlation coefficients was 0.95 ± 0.02 (range, 0.89–0.97) for FB. The maximal phase shift was 0.13 s for FB. The mean ± SD of the correlation coefficients was 0.97 ± 0.02 (range, 0.93–0.99) for audio coaching. The mean correlation coefficient between these groups was also significant ($p < .01$). Figure 3a,b shows a diagram of the lung tumor displacement vs. time and a scatterplot of the lung tumor displacement vs. abdominal displacement for Patient 5 in Session 3, respectively. Of all the patients, the greatest improvement in the correlation coefficient was observed for Patient 5. Using audio coaching, the average SI tumor displacement increased from 9.4 to 18.5 mm (Fig. 3a), and the observed phase shift between the tumor motion and abdominal displacement was reduced (Fig. 3b).

The SI lung tumor position mismatches for FB and audio coaching are summarized in Table 3. These mismatches persisted and varied daily. Although the SI lung tumor position mismatches became larger in 75% of all sessions with audio coaching compared with FB, no significant difference was observed between these groups ($p = .01$). The SI lung tumor position mismatches were within an average of 1.70 mm for FB and 2.09 mm for audio coaching.

DISCUSSION

Treatment planning and dose delivery of external gated RT requires intra- and interfraction reproducibility of the tumor–surrogate relationship (13, 14, 19) and stability of the intra- and interfraction target position (22) during the treatment course. In the present study, we evaluated the effect of audio

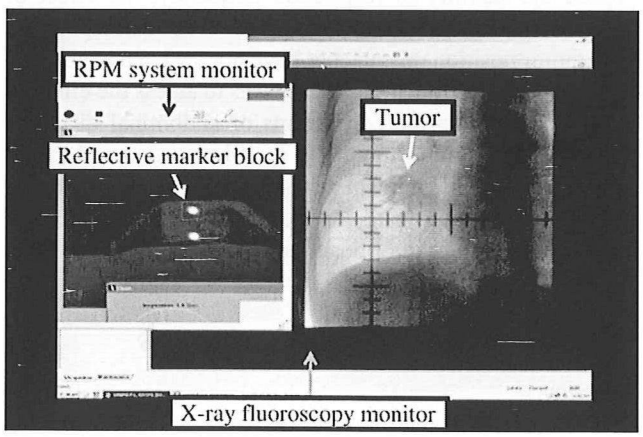

Fig. 1. Parallel display of real-time positioning management system monitor showing abdominal motion using reflective marker block and chest fluoroscopic image, which can project tumor shape from anterior of patient.

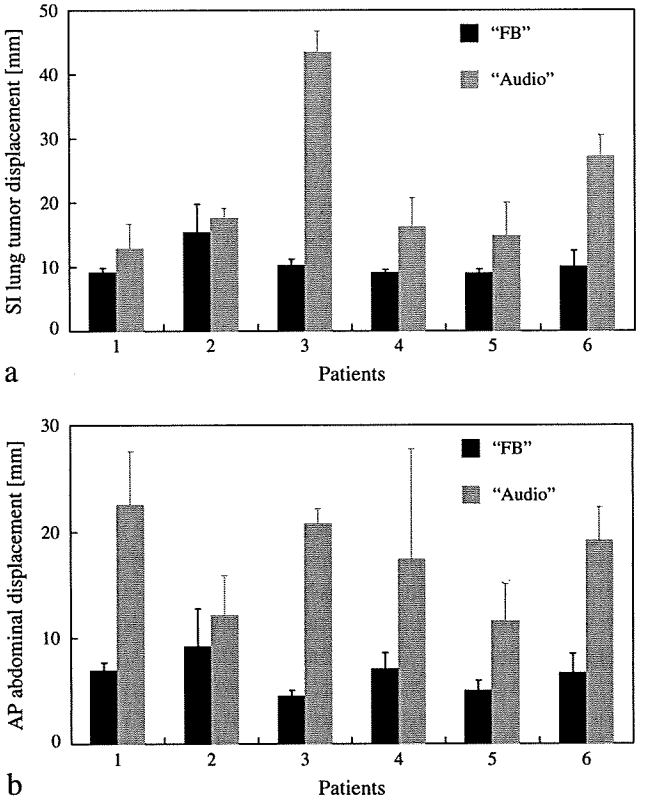

Fig. 2. (a) Superoinferior tumor displacement and (b) anteroposterior abdominal displacement averaged for consecutive respiratory cycles with and without audio coaching. Error bars show standard deviation.

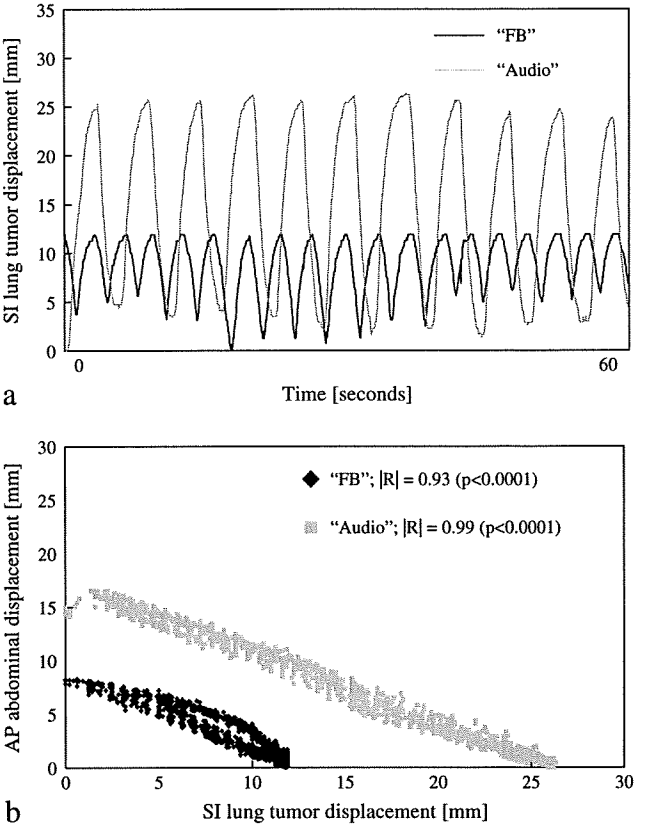

Fig. 3. (a) Time course of superoinferior lung tumor position and (b) scatterplot showing relationship with abdominal position for Patient 5 in Session 3, with and without audio coaching.

coaching on the correlation of abdominal displacement with lung tumor motion and SI lung tumor position mismatches using a template matching technique. Audio coaching generally led to an increase in the abdominal and lung tumor displacements in the AP and SI direction, respectively. Although a significant difference was shown in the tumor–abdominal correlation between the audio coaching and FB, the SI lung tumor position mismatches became slightly larger with audio coaching than without audio coaching.

A strong correlation between the external surrogate signals and internal tumor motion is required to perform external gated RT securely. Ahn *et al.* (13) used skin markers as the external surrogate signal and verified the relationship between the movement of the skin and the target organ. They showed a strong correlation (mean ± SD, 0.77 ± 0.12) between the skin and tumor movement, especially for sites in the lower lung. Hoisak *et al.* (14) assessed the correlation of abdominal displacement with the tumor motion as seen on X-ray fluoroscopy for multiple days, and reported a correlation range of 0.39–0.98. Because of the smaller phase shifts in our study than in their study, high correlation coefficients were obtained with FB. A possible cause of the phase shifts included the breathing type. Two main types of breathing exist: chest breathing and abdominal breathing. We estimated that the tumor and abdominal skin surface might move concurrently in abdominal breathing, which would result in reducing the phase shifts between the lung tumor and abdominal skin surface. In contrast, a slight time lag would occur between the abdominal skin surface and the lung tumor motion in chest breathing. If chest breathing is directed to abdominal breathing, external gated RT using an abdominal motion signal would then be performed more accurately because of the better tumor–abdominal correlation. In addition, patients tended to breathe consciously during audio coaching; thus, chest breathing might switch to abdominal breathing (23). The diaphragm is an important muscle and controls abdominal and lung tumor movement during respiration. Using audio coaching, the relaxation/contraction of the diaphragm might be stimulated. Thus, it is possible that

Table 2. Tumor–abdominal motion correlation coefficients throughout measurement sessions

	Free breathing			Audio coaching		
Pt. No.	Session 1	Session 2	Session 3	Session 1	Session 2	Session 3
1	0.97	0.97	0.97	NA	0.98	0.99
2	0.96	0.96	0.95	0.96	0.98	0.98
3	0.97	0.96	0.94	0.99	0.98	0.99
4	0.93	0.95	0.94	0.94	0.93	0.94
5	0.89	0.96	0.93	NA	0.99	0.99
6	0.93	0.97	0.97	0.95	0.96	0.97

Abbreviations: Pt. No. = patient number; NA = not available (patient did not participate in measurement session).

Table 3. Mean SI lung tumor position mismatches with and without audio coaching

	Free breathing (mm)			Audio coaching (mm)		
Pt. No.	Session 1	Session 2	Session 3	Session 1	Session 2	Session 3
1	0.49 (0.47–0.52)	0.71 (0.68–0.73)	0.61 (0.59–0.64)	NA	0.52 (0.49–0.54)	0.71 (0.67–0.75)
2	1.70 (1.63–1.77)	0.88 (0.85–0.92)	1.00 (0.95–1.06)	1.66 (1.58–1.74)	1.12 (1.08–1.17)	0.53 (0.50–0.55)
3	1.21 (1.15–1.26)	1.26 (1.18–1.33)	0.61 (0.58–0.64)	1.60 (1.51–1.69)	1.70 (1.60–1.79)	1.18 (1.13–1.24)
4	0.44 (0.42–0.46)	0.73 (0.70–0.76)	0.67 (0.64–0.70)	1.49 (1.40–1.57)	1.82 (1.74–1.89)	0.93 (0.89–0.97)
5	0.84 (0.80–0.88)	0.53 (0.50–0.55)	0.86 (0.86–0.90)	NA	0.57 (0.54–0.60)	0.69 (0.65–0.72)
6	0.77 (0.73–0.81)	0.45 (0.42–0.48)	0.69 (0.66–0.71)	1.30 (1.24–1.37)	1.72 (1.61–1.82)	2.09 (1.98–2.20)

Abbreviations: SI = superoinferior; other abbreviations as in Table 2.
Data in parentheses are 99% confidence intervals.

stimulation might have resulted in amplification of the lung tumor and abdominal displacement in the present study.

Although audio coaching significantly improved the tumor–abdominal motion correlation ($p < .01$), the total tumor movement as measured during the full respiratory cycle became larger, comparable with the results of Haasbeek *et al.* (24). Audio coaching not only stimulated tumor movement (Fig. 2a), but often resulted in a slight increase in the differences between the predicted and measured lung tumor position in the SI direction (Table 3). For example, the mismatch was an average of ≥1 mm for 62.5% of audio coaching compared with 22.2% of FB. Seppenwoolde *et al.* (25) used implanted fiducial markers and reported that the lung tumor moved with a degree of deviation from the mean trajectory position. Because the tumor largely moves during the respiration cycle, the deviation would be more pronounced. This would result in an increase in the SI lung tumor position mismatches. In contrast, audio coaching reduced the SI lung tumor position mismatches in 25% of the sessions. Thus, it was difficult to identify which factor, phase shift or tumor displacement, predominantly affected the SI lung tumor position mismatches in the present study. Additional margins or expansion of the gating window would be needed to compensate for these uncertainties in clinical practice.

An additional issue in external gated RT with audio coaching alone is an increase in the SI lung tumor position mismatches resulting from the larger motion range of the lung tumor. Haasbeek *et al.* (24) also concluded that differences in lung tumor position >5 mm between FB and audio coaching were detected in ≤56% of lung tumors with a motion range >10 mm (24). On the basis of our results, and theirs, it is more important to manage respiratory motion when applying audio coaching alone to external gated RT. As one of the methods to reduce SI lung tumor position mismatches, audiovisual biofeedback is expected to be suitable (26). The advantage of audiovisual biofeedback compared with audio coaching is that patients can maintain an arbitrary depth of respiration. Thus, it should result in a decrease in the mismatches between the predicted and measured lung tumor position.

CONCLUSION

Audio coaching served to increase the degree of correlation and made it more reproducible. In addition, the phase shifts between the tumor motion and abdominal displacement improved. All patients breathed more deeply, and the SI lung tumor position mismatches became slightly larger with audio coaching than without audio coaching.

REFERENCES

1. International Commission on Radiation Units and Measurements. Prescribing, recording and reporting photon beam therapy: Report No. 62 (supplement to ICRU report No. 50. Bethesda: ICRU; 1999.
2. Negoro Y, Nagata Y, Aoki T, *et al.* The effectiveness of an immobilization device in conformal radiotherapy for lung tumor: Reduction of respiratory tumor movement and evaluation of the daily setup accuracy. *Int J Radiat Oncol Biol Phys* 2001; 50:889–898.
3. Hanley J, Debois MM, Mah D, *et al.* Deep inspiration breath-hold technique for lung tumors: The potential value of target immobilization reduced lung density in dose escalation. *Int J Radiat Oncol Biol Phys* 1999;45:603–611.
4. Rosenzweig KE, Hanley J, Mah D, *et al.* The deep inspiration breath-hold technique in the treatment of inoperable non small-cell lung cancer. *Int J Radiat Oncol Biol Phys* 2000;48: 81–87.
5. Mah D, Hanley J, Rosenzweig KE, *et al.* Technical aspects of the deep inspiration breath-hold technique in the treatment of thoracic cancer. *Int J Radiat Oncol Biol Phys* 2000;48: 1175–1185.
6. Ramsey CR, Cordrey IL, Oliver AL. A comparison of beam characteristics for gated and nongated clinical x-ray beams. *Med Phys* 1999;26:2086–2091.
7. Paoli J, Rosenzweig KE, Yorke E, *et al.* Comparison of different respiratory levels in the treatment of lung cancer: Implications for gated treatment. *Int J Radiat Oncol Biol Phys* 1999;45: 386–387.
8. Shirato H, Shimizu S, Kunieda T, *et al.* Physical aspects of a real-time tracking system for gated radiotherapy. *Int J Radiat Oncol Biol Phys* 2000;48:1187–1195.
9. Ford EC, Mageras GS, Yorke E, *et al.* Evaluation of respiratory movement during gated radiotherapy using film and electronic portal imaging. *Int J Radiat Oncol Biol Phys* 2002;52:522–531.
10. Berson AM, Emery R, Rodriguez L, *et al.* Clinical experience using respiratory gated radiation therapy: Comparison of free-breathing and breath-hold techniques. *Int J Radiat Oncol Biol Phys* 2004;60:419–426.

11. Keall PJ, Kini V, Vedam SS, *et al.* Motion adaptive X-ray therapy: A feasibility study. *Phys Med Biol* 2001;46:1–10.
12. Keall PJ, Joshi S, Vedam SS, *et al.* Four-dimensional radiotherapy planning for DMLC-based respiratory motion tracking. *Med Phys* 2005;32:942–951.
13. Ahn S, Yi B, Suh Y, *et al.* A feasibility study on the prediction of tumour location in the lung from skin motion. *Br J Radiol* 2004;77:588–596.
14. Hoisak JD, Sixel KE, Tirona R, *et al.* Correlation of lung tumor motion with external surrogate indicators of respiration. *Int J Radiat Oncol Biol Phys* 2004;60:1298–1306.
15. Vedam SS, Keall PJ, Kini V, *et al.* Determining parameters for respiratory gated radiotherapy. *Med Phys* 2001;28:2139–2146.
16. Ozhasoglu C, Murphy MJ. Issues in respiratory motion compensation during external-beam radiotherapy. *Int J Radiat Oncol Biol Phys* 2002;52:1389–1399.
17. Ionascu D, Jiang SB, Nishioka S, *et al.* Internal-external correlation investigations of respiratory induced motion of lung tumors. *Med Phys* 2007;34:3893–3903.
18. Mageras GS, Yorke ED, Rosenzweig A, *et al.* Fluoroscopic evaluation of diaphragmatic motion reduction with a respiratory gated radiotherapy system. *J Appl Clin Med Phys* 2001;2: 191–200.
19. Nakamura M, Narita Y, Matsuo Y, *et al.* Correlative analysis of abdominal motion with lung tumor motion for non-invasive respiratory gated radiotherapy. *J Jpn Soc Ther Radiol Oncol* 2008;20:119–125.
20. Kini VR, Vedam SS, Keall PJ, *et al.* Patient training in respiratory-gated radiotherapy. *Med Dosim* 2003;28:7–11.
21. Kubo HD, Wang L. Introduction of audio gating to further reduce organ motion in breathing synchronized radiotherapy. *Med Phys* 2002;29:345–350.
22. Juhler NT, Korreman SS, Pedersen AN, *et al.* Intra- and interfraction breathing variations during curative radiotherapy for lung cancer. *Radiother Oncol* 2007;84:40–48.
23. Neicu T, Berbeco R, Wolfgang J, *et al.* Synchronized moving aperture radiation therapy (SMART): Improvement of breathing pattern reproducibility using respiratory coaching. *Phys Med Biol* 2006;51:617–636.
24. Haasbeek CJA, Spoelstra FOB, Lagerwaard FJ, *et al.* Impact of audio-coaching on the position of lung tumors. *Int J Radiat Oncol Biol Phys* 2008;71:1118–1123.
25. Seppenwoolde Y, Shirato H, Kitamura K, *et al.* Precise and real-time measurement of 3D tumor motion in lung due to breathing and heartbeat, measured during radiotherapy. *Int J Radiat Oncol Biol Phys* 2002;53:822–834.
26. George R, Chung TD, Vedam SS, *et al.* Audio-visual biofeedback for respiratory-gated radiotherapy: Impact of audio coaching and audio-visual biofeedback on respiratory-gated radiotherapy. *Int J Radiat Oncol Biol Phys* 2006;65:924–933.

Impact of motion velocity on four-dimensional target volumes: A phantom study

Mitsuhiro Nakamura,[a] Yuichiro Narita, Akira Sawada, and Kiyotomo Matsugi
Department of Radiation Oncology and Image-Applied Therapy, Graduate School of Medicine, Kyoto University, 54 Kawahara-cho, Shogoin, Sakyo-ku, Kyoto 606-8507, Japan

Manabu Nakata
Clinical Radiology Service Division, Kyoto University Hospital, Kyoto 606-8507, Japan

Yukinori Matsuo, Takashi Mizowaki, and Masahiro Hiraoka
Department of Radiation Oncology and Image-Applied Therapy, Graduate School of Medicine, Kyoto University, 54 Kawahara-cho, Shogoin, Sakyo-ku Kyoto 606-8507, Japan

(Received 27 September 2008; revised 6 February 2009; accepted for publication 5 March 2009; published 10 April 2009)

This study aims to assess the impact of motion velocity that may cause motion artifacts on target volumes (TVs) using a one-dimensional moving phantom. A 20 mm diameter spherical object embedded in a QUASAR™ phantom sinusoidally moved with approximately 5.0 or 10.0 mm amplitude (A) along the longitudinal axis of the computed tomography (CT) couch. The motion period was manually set in the range of 2.0–10.0 s at approximately 2.0 s interval. Four-dimensional (4D) CT images were acquired by a four-slice CT scanner (LightSpeed RT; General Electric Medical Systems, Waukesha, WI) with a slice thickness of 1.25 mm in axial cine mode. The minimum gantry rotation of 1.0 s was employed to achieve the maximum in-slice temporal resolution. Projection data over a full gantry rotation (1.0 s) were used for image reconstruction. Reflective marker position was recorded by the real-time positioning management system (Varian Medical Systems, Palo Alto, CA). ADVANTAGE 4D software exported ten respiratory phase volumes and the maximum intensity volume generated from all reconstructed data (MIV). The threshold to obtain static object volume (V_0, 4.19 ml) was used to automatically segment TVs on CT images, and then the union of TVs on 4D CT images (TV_{4D}) was constructed. TVs on MIV (TV_{MIV}) were also segmented by the threshold that can determine the area occupied within the central slice of TV_{MIV}. The maximum motion velocity for each phase bin was calculated using the actual averaged motion period displayed on ADVANTAGE 4D software (T), the range of phases used to construct the target phase bin (phase range), and a mathematical model of sinusoidal function. Each volume size and the motion range of TV in the cranial-caudal (CC) direction were measured. Subsequently, cross-correlation coefficients between TV size and motion velocity as well as phase range were calculated. Both misalignment and motion-blurring artifacts were caused by high motion velocity. Less than 6% phase range was needed to construct the 4D CT data set, except for T of 2.0 s. While the positional differences between the TV and ideal centroid in the CC direction were within the voxel size for $T \geq 6.0$ s, the differences were up to 2.43 and 4.15 mm for $(A,T) = (5.0\ \text{mm}, 2.0\ \text{s})$ and (10.0 mm, 2.0 s), respectively. The maximum volumetric deviations between TV sizes and V_0 were 43.68% and 91.41% for A of 5.0 and 10.0 mm, respectively. TV_{MIV} sizes were slightly larger than TV_{4D} sizes. Volumetric deviation between TV size and V_0 had a stronger correlation with motion velocity rather than phase range. This phantom study demonstrated that motion artifacts were substantially reduced when the phantom moved longitudinally at low motion velocity during 4D CT image acquisition; therefore, geometrical uncertainties due to motion artifacts should be recognized when determining TVs, especially with a fast period. [DOI: 10.1118/1.3110073]

Key words: 4D CT, phase-based sorting, motion velocity, motion arifacts

I. INTRODUCTION

It has been recognized that motion artifacts can sometimes be introduced if organ motion occurs during computed tomography (CT) data acquisition.[1–3] Motion artifacts give an inaccurate representation of the shape, volume size, and position of normal organs and target volumes (TVs), leading to crucial delineation errors in treatment planning. Such motion artifacts can be mitigated by breath-hold[4–6] and four-dimensional (4D) CT.[7–13]

Recently, 4D CT has been increasingly utilized in clinical practice. With 4D CT images, tumor and organ motion information is directly incorporated into treatment planning and thus can help decide on appropriate treatment delivery

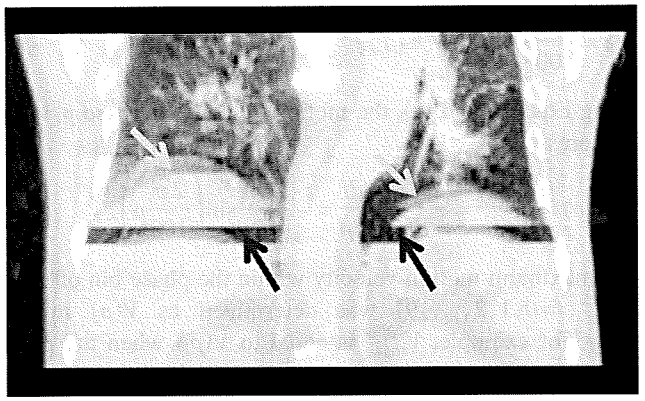

FIG. 1. Examples of misalignment artifacts and motion-blurring artifacts. Upper arrows show misalignment artifacts resulting from mismatches in respiratory phase between adjacent couch positions. The diaphragm is imaged as two disconnected parts. Lower arrows show motion-blurring artifacts. The edges of the diaphragm become blurred due to poor temporal resolution of the CT scanner to the velocity of the diaphragm.

techniques.[11–13] The current approaches of 4D CT acquisition can be accomplished by both oversampled CT data acquisition and retrospective sorting using simultaneously recorded respiratory signals during CT scanning. Respiratory signals are based either on respiratory phase or abdominal displacement. There are two main approaches for 4D CT acquisition: Helical approach[7–9] and cine approach.[10–13] In the helical approach, overlapping projection data are acquired with a very low helical pitch. The helical pitch is sufficiently low such that projection data for a full respiratory cycle are acquired per slice location. Respiratory states of interest are selected prior to image reconstruction. Projection data corresponding to the selected respiratory states are sorted to reconstruct an image, and then a three-dimensional (3D) data set in these respiratory states is generated. On the other hand, the cine approach can be achieved by repeated image acquisition per couch position in axial scan mode. Cine duration is set to more than the maximum observed respiratory period in order to acquire image data throughout the entire respiratory cycle. Multiple images are reconstructed at each couch position. The reconstructed CT images are sorted according to respiratory signals. Finally, 4D CT data sets are generated by assembling CT images that have the nearest respiratory phase or abdominal displacement to the target one for each position.

Several investigators reported that motion artifacts can still be induced even with 4D CT imaging.[14–16] Motion artifacts can be categorized as misalignment artifacts and motion-blurring artifacts (Fig. 1). The quality and integrity of 4D CT images are impaired by variations in respiratory patterns during data acquisition.[15] For example, irregular respiratory patterns make it difficult for the real-time positioning management (RPM) system (Varian Medical Systems, Palo Alto, CA) to determine the accurate respiratory phases.[15–18] As a result, misalignment artifacts often occur at an interface between adjacent couch positions, a possible cause of which is mismatches of respiratory phases between them. On the other hand, motion-blurring artifacts appear when organ motion is faster than the gantry rotational speed. The edges of an anatomical structure become blurred due to poor temporal resolution of CT scanners to the velocity of the structure.

In spite of regular respiratory pattern, we experienced some clinical cases in which severe motion artifacts were observed. Although respiratory velocity has been suggested as another factor of motion artifacts on 4D CT images,[13] quantitative evaluation has not yet been performed by the cine approach. In addition, severe motion artifacts would reduce the accuracy of TVs derived from all phases of 4D CT (TV_{4D}) as well as those on maximum intensity volume (TV_{MIV}; MIV=maximum intensity volume). The purpose of this study was to assess the impact of motion velocity that may cause motion artifacts on TVs using a one-dimensional moving phantom and the cine approach.

II. MATERIALS AND METHODS

II.A. Phantom and 4D CT data acquisition

A 20 mm diameter spherical object [CT number of around 350 Hounsfield units (HU)] embedded in a QUASAR™ phantom sinusoidally moved with approximately 5.0 and 10.0 mm amplitude (A) along the longitudinal axis of the CT couch. A reflective marker block was tightly attached to the QUASAR™ phantom. Mechanical linkage synchronously moved the marker block up and down while the phantom moved longitudinally. The object motion period (T_0) was manually set in the range of 2.0–10.0 s at approximately 2.0 s interval. 4D CT images were acquired by a four-slice CT scanner (LightSpeed RT; General Electric Medical Systems, Waukesha, WI) with a slice thickness of 1.25 mm in axial cine mode. Reflective marker position was recorded by the RPM system version 1.6. Scan length was set to the full extent of object motion. Scan parameters were 120 kV, 100 mA, $T_0+2.0$ s cine duration time of the scan in each couch position (T_{cine}), and 0.25 s cine interval between images (T_{images}). The T_{images} parameter controls temporal spacing between two consecutive images reconstructed at the same scan position. Interscan delay (ISD) was set to prevent marker vibration resulting from couch movement and to synchronize scan timing in each couch position. The value of ISD was 2.0 s for T_0 of 2.0 s and $2T_0-T_{\text{cine}}$ s for $T_0 \geq 4.0$ s, respectively. In general, in-slice artifacts appear when an object moves during projection data acquisition.[13] The minimum gantry rotation of 1.0 s was employed to achieve the maximum in-slice temporal resolution. Projection data over a full gantry rotation (1.0 s) were used for image reconstruction. To assess reproducibility, measurements were repeated three times for each condition, combining A and T_0.

The RPM system calculated a phase at each point of a respiratory trace, where 0% corresponding to the inhalation peak and 50% to the midpoint between consecutive inhalation peaks. All CT slices and RPM respiratory data file were transferred to an ADVANTAGE 4D workstation (General Electric Medical Systems, Waukesha, WI). ADVANTAGE 4D software read all CT slices as well as the corresponding RPM respiratory data file, assigned a phase to each CT slice according to the temporal correlation between the RPM trace

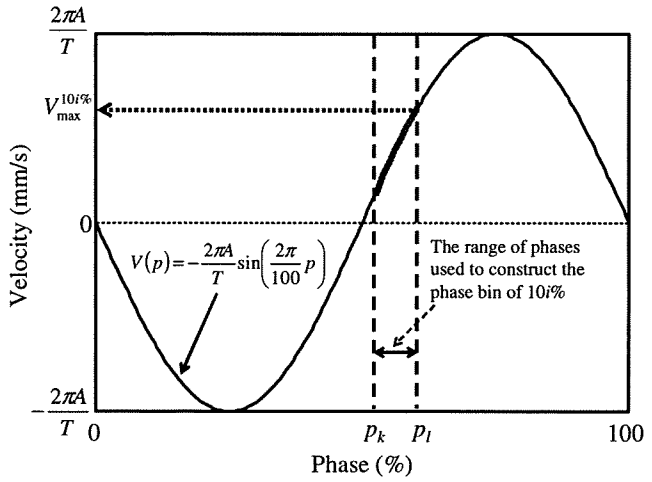

FIG. 2. Diagram of how to calculate $V_{max}^{10i\%}$. When the phase range of p_k to p_l for constructing the phase bin of $10i\%$ is given, $V_{max}^{10i\%}$ is equivalent to $V(p_l)$.

and CT data acquisition, and exported ten respiratory phase volumes, evenly distributed over a respiratory cycle.[11–13] The MIV was also generated from all reconstructed data.[19]

II.B. Motion velocity calculation

The actual averaged motion period (T) was calculated from RPM data and displayed on ADVANTAGE 4D software. Both T and the range of phases used to construct the target phase bin (phase range) were used as parameters for calculating motion velocity. Object position as a function of time t is expressed as

$$A(t)=A\cos\left(\frac{2\pi}{T}t\right), \tag{1}$$

where $A(t)$ is the object position at time t. The relationship between phase p as a percentage ($0\le p\le 100$) and time t in seconds is as follows:

$$t=\frac{p}{100}T \quad (0\le t\le T). \tag{2}$$

Using Eqs. (1) and (2), the motion velocity in phase $p[V(p)]$ is expressed as

$$V(p)=\frac{dA(t)}{dp}=\frac{dA(t)}{dt}\cdot\frac{dt}{dp}=-\frac{2\pi A}{T}\sin\left(\frac{2\pi}{100}p\right). \tag{3}$$

The maximum motion velocity within the phase bin of $10i\%$ ($V_{max}^{10i\%}; i=0,1,2,\ldots,9$) was determined as $V(p)$ in this study; for example, $V_{max}^{10i\%}$ is equal to $V(p_l)$ when the phase range of p_k to p_l for constructing the phase bin of $10i\%$ on an ADVANTAGE 4D workstation is given (Fig. 2).

II.C. Target volume definition and analysis

All CT data sets were imported into a commercially available 3D radiation treatment planning system (ECLIPSE 7.3.10; Varian, Palo Alto, CA). To eliminate inter- and intraobserver variations, the threshold to obtain static object volume (V_0, 4.19 ml) was used to automatically segment TVs on CT images, and then TV_{4D} was constructed. TV_{MIV} was also segmented by the threshold that can determine the area occupied within the central slice of TV_{MIV}.

Each volume size and the motion range of TV in the cranial-caudal (CC) direction were measured. Subsequently, cross-correlation coefficients between TV size and motion velocity as well as phase range were calculated.

The volume sizes of TV_{4D} and TV_{MIV} were compared to the theoretical volume size (V_{theory}) calculated with the following Eq. (4):

$$V_{theory}=\frac{4\pi r^3}{3}+2\pi r^2 A, \tag{4}$$

where r denotes the radius of the spherical object. In Eq. (4), we assume that r is equal to 10 mm, and then V_{theory} were 7.33 and 10.47 ml for A of 5.0 and 10.0 mm, respectively.

TABLE I. The range of phases used to construct the phase bin for A of 5.0 mm in measurement 1. Data are represented as differences from the target phase of $10i\%$ ($i=0,1,2,\ldots,9$). The data in bold show that the phase bins do not include phases of $10i\%$: SD=standard deviation.

Phase bin	T=2.0 s	T=4.0 s	T=6.0 s	T=8.0 s	T=9.9 s
0%	**3%–5%**	−3%–2%	−2%–1%	−1%–2%	−1%–1%
10%	−7%–5%	−1%–3%	−2%–2%	−1%–1%	−1%–1%
20%	**−5%–3%**	−3%–3%	−2%–1%	−1%–1%	−1%–1%
30%	**−3%–1%**	−2%–1%	−2%–2%	−1%–1%	−1%–1%
40%	**1%–2%**	−3%–2%	−2%–1%	−2%–1%	−1%–1%
50%	**3%–5%**	−3%–0%	−2%–1%	−2%–1%	−1%–1%
60%	−6%–6%	−1%–3%	−2%–2%	−1%–1%	−1%–1%
70%	**−3%–2%**	−2%–3%	−2%–2%	−2%–1%	−1%–1%
80%	−2%–0%	−3%–1%	−2%–2%	−2%–1%	−1%–1%
90%	**1%–2%**	−3%–2%	−2%–1%	−1%–1%	−1%–1%
Mean (%)	3.7	4.4	3.5	2.5	2.0
SD (%)	4.4	1.0	0.5	0.5	0.0

TABLE II. The range of phases used to construct the phase bin for A of 10.0 mm in measurement 1. Data are represented as differences from the target phase of $10i\%$ (i=0,1,2,...,9): SD=standard deviation.

Phase bin	T=2.0 s	T=4.0 s	T=6.0 s	T=8.1 s	T=10.0 s
0%	−7%–5%	−3%–2%	−1%–1%	−2%–1%	−1%–1%
10%	−5%–5%	−2%–3%	−1%–2%	−2%–1%	−1%–1%
20%	−5%–5%	−3%–3%	−1%–1%	−2%–2%	−1%–0%
30%	−6%–6%	−3%–3%	−2%–1%	−2%–1%	−1%–1%
40%	−5%–5%	−3%–2%	−2%–1%	−2%–1%	−1%–1%
50%	−7%–5%	−2%–2%	−1%–0%	−1%–1%	−1%–1%
60%	−5%–5%	−3%–3%	−2%–1%	−2%–1%	−1%–1%
70%	−5%–5%	−3%–3%	−1%–1%	−2%–1%	−1%–1%
80%	−5%–6%	−3%–3%	−2%–1%	−2%–1%	−1%–1%
90%	−5%–5%	−3%–2%	−2%–1%	−2%–1%	−1%–1%
Mean (%)	10.7	5.4	2.5	3.0	1.9
SD (%)	0.9	0.7	0.7	0.5	0.3

III. RESULTS

III.A. Phase range for constructing phase bin

The phase range in measurement 1 is shown in Tables I and II. The data were represented as differences to the target phase. Less than 6% phase range was needed to construct the 4D CT data set, except for T of 2.0 s. The standard deviation (SD) of the phase range became smaller as the period slowed. The data in bold showed that the phase bins did not include phases of $10i\%$ (Table I). A similar tendency was shown in all measurements.

III.B. Target volume analysis

Axial images in 10% phase are displayed in Fig. 3. The central slice of the imaged object is located at zero position in each motion state. Figure 4 shows central coronal images through segmentation of the object for ten different motion phases imaged with 4D CT. The motion sequence advances from left to right. By visual assessment, in-slice, motion-blurring, and misalignment artifacts were evident for (A,T) =(10.0 mm,2.0 s) (Fig. 3, fourth line and Fig. 4, third line). In contrast, the images through the object were almost perfectly circular for (A,T)=(5.0 mm,9.9 s) (Fig. 3, third line and Fig. 4, second line).

The ratios of TV size to V_0 are plotted as a function of phase in Fig. 5. TV sizes were larger than V_0 by up to 43.68% and 91.41% for A of 5.0 and 10.0 mm, respectively. The amplification of TV displacement resulted in large volumetric deviations. As the motion phase approached 0% and 50% phases, TV sizes were closer to V_0. On the other hand,

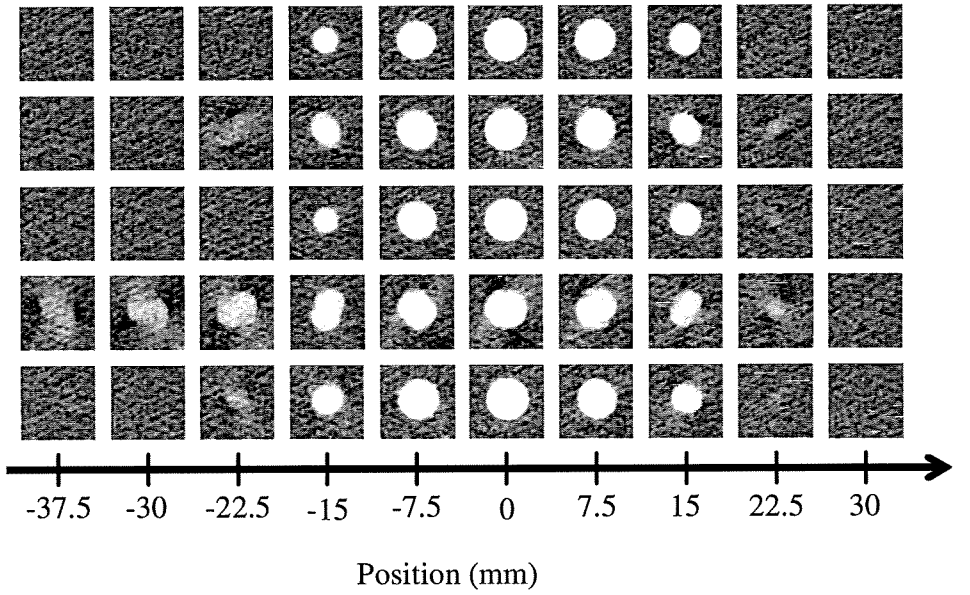

FIG. 3. Axial images in 10% phase (window width: 170 HU and window level: 170 HU). The central slice of the imaged object is located at zero position in each motion state. Top: Static. Second line: (A,T)=(5.0 mm,2.0 s). Third line: (A,T)=(5.0 mm,9.9 s). The effects of in-slice artifacts are almost diminished. Fourth line: (A,T)=(10.0 mm,2.0 s). In-slice artifacts are noticeable, especially at the sphere pole. Bottom: (A,T)=(10.0 mm,10.0 s).

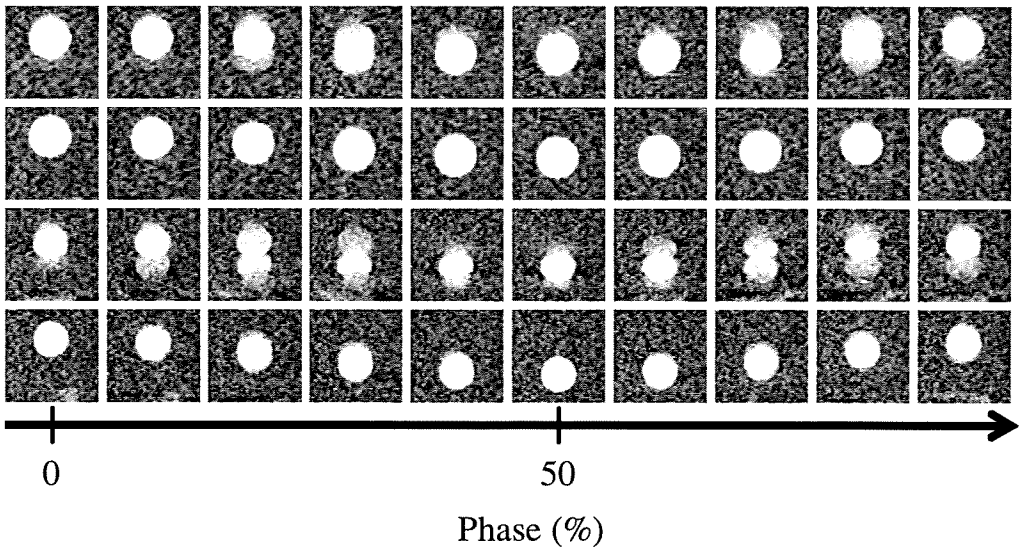

FIG. 4. Coronal images of a spherical object (window width: 170 HU and window level: 170 HU). The motion sequence advances from left to right. Top: $(A,T)=(5.0\text{ mm},2.0\text{ s})$ Second line: $(A,T)=(5.0\text{ mm},9.9\text{ s})$. Images through the object are almost perfectly circular. Third line: $(A,T)=(10.0\text{ mm},2.0\text{ s})$. Motion-blurring artifacts are observed in all motion phases, and misalignment artifacts are evident near midexhalation and midinhalation. Bottom: $(A,T)=(10.0\text{ mm},10.0\text{ s})$.

amplitude reductions were pronounced near 0% and 50% phases (Fig. 6). While positional differences between the TV and ideal centroid in the CC direction were within the voxel size for $T\geq 6.0$ s, the differences were up to 2.43 and 4.15 mm for $(A,T)=(5.0\text{ mm},2.0\text{ s})$ and (10.0 mm, 2.0 s), respectively.

Figure 7 shows volumetric deviations between the TV size and V_0 as a function of phase range. Even with a phase range of 1%, volumetric deviation was 38.19% for A of 5.0 mm. Linear correlation coefficients between the phase range and TV size were 0.38 (slope=1.87 and intercept=4.20) and 0.73 (slope=4.21 and intercept=3.27) for A of 5.0 and 10.0 mm, respectively.

The correlation of volumetric deviation with motion velocity was stronger than the phase range (Fig. 8). Linear correlation coefficients between motion velocity and TV size were 0.91 (slope=2.35 and intercept=−1.54) and 0.92 (slope=1.99 and intercept=1.50) for A of 5.0 and 10.0 mm, respectively. The volumetric deviation of ±2% was achieved with a tolerance of 2.0 mm/s.

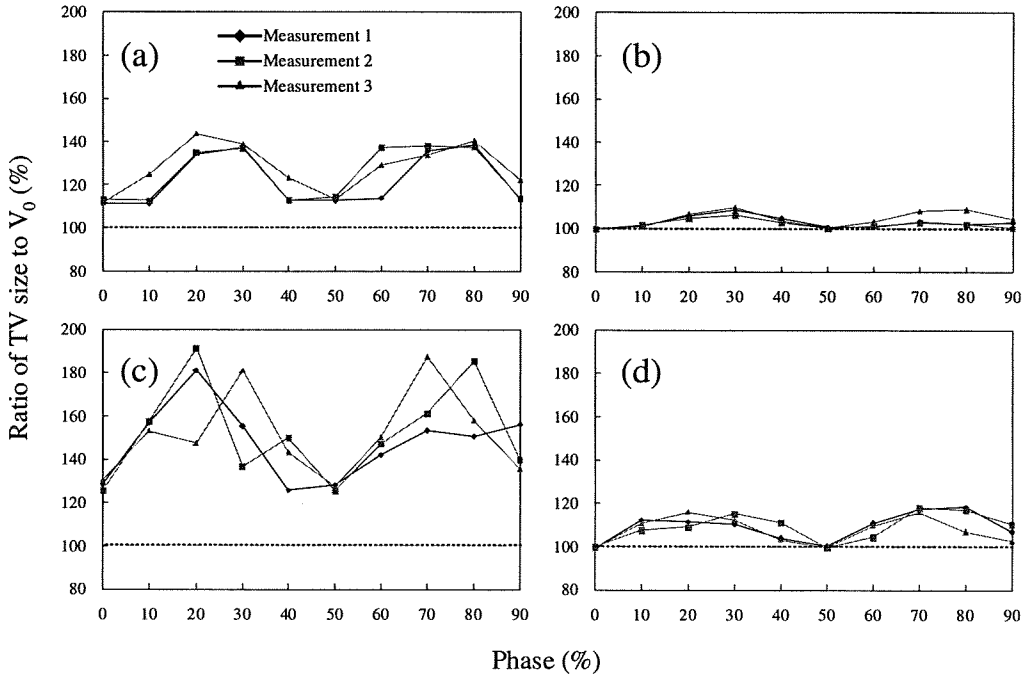

FIG. 5. Ratio of TV size to V_0: (a) $(A,T)=(5.0\text{ mm},2.0\text{ s})$, (b) $(A,T)=(5.0\text{ mm},9.9\text{ s})$, (c) $(A,T)=(10.0\text{ mm},2.0\text{ s})$, and (d) $(A,T)=(10.0\text{ mm},10.0\text{ s})$.